Lawrence Livermore National Laboratory

LLNL-JRNL-2001408

Benchmark microgravity experiments and computations for 3D dendritic-array stability in directional solidification

K. Ji

March 2025

Disclaimer

This work performed under the auspices of the U.S. Department of Energy by Lawrence Livermore National Laboratory under Contract DE-AC52-07NA27344.

Release #: LLNL-JRNL-2001408

Benchmark microgravity experiments and computations for 3D dendritic-array stability in directional solidification

Mehdi Medjkoune,[1] Trevor Lyons,[2] Fátima L. Mota,[1] Jiefu Tian,[2] Kaihua Ji,[2, 3] Louise Littles,[4] Alain Karma,[2] and Nathalie Bergeon,[1]

[1]*Aix Marseille Univ, CNRS, IM2NP, Marseille, France*
[2]*Department of Physics and Center for Interdisciplinary research on Complex Systems, Northeastern University, Boston MA 02115, USA*
[3]*Materials Science Division, Lawrence Livermore National Laboratory, Livermore, CA 94550, USA*
[4]*Marshall Space Flight Center, Huntsville, USA*

(Dated: February 7, 2024)

Abstract

In this study, we present a comprehensive quantitative analysis of stability bands for dendritic arrays during directional solidification of a transparent succinonitrile-0.46 wt% camphor alloy, spanning a broad range of pulling velocities. Taking advantage of the microgravity environment aboard the International Space Station where most convection effects are suppressed, we obtain unique measurements that quantify the stable primary spacing range of spatially extended three-dimensional dendritic array structures under purely diffusive growth conditions. Through carefully designed velocity jump experiments and detailed examination of sub-grain boundary dynamics, we characterize key instabilities, including elimination and tertiary branching, shedding new light on the mechanisms governing dynamic dendritic spacing selection in extended 3D arrays. Phase field simulations are performed to characterize the stability limits of dendritic array structures for quantitative comparison with the flight experiments. Although the simulations capture general trends, significant deviations are noted at the upper stability boundary, indicating the influence of additional, unexplored factors. These findings contribute to a deeper understanding of dendritic growth dynamics and offer valuable benchmark data that could aid in refining predictive models and improving control of dendritic microstructures in metallurgical applications.

Keywords: Directional solidification, Microgravity experiment, Transparent alloy, Phase field simulations, Dendritic Spacing

1 Introduction

Solidification is the primary step in processing most metallic alloys. The microstructure formed during this phase significantly influences the properties, performance, and longevity of metal castings. The typical and most common morphology in cast alloys is dendritic structures [1-3] which are tree-like formations with primary and secondary branches. These dendrites exhibit various key length scales, such as primary and secondary spacings or dendrite tip radius. Spacings directly impact the mechanical properties of the metal, including tensile strength, yield strength, permeability or corrosion resistance [4-13]. While the selection of a unique dendrite tip radius is unambiguously determined by the microscopic solvability theory [14-18] for a set of given pulling rate V_p, thermal gradient G and solute concentration C, the primary spacing λ shows a wide accessible range under similar solidification conditions for which the system is stable. In fact, the dynamical selection of the primary cell/dendrite spacing λ has been extensively studied both theoretically [19-40] and experimentally [20, 21, 24, 41-52]. It is well-established that spatially periodic array structures are stable over a wide range of spacing bounded, for dendritic arrays, by elimination at small spacing ($\lambda < \lambda_{el}$) and tertiary branching at large spacing ($\lambda > \lambda_{br}$).

It is also known that the dynamical selection of the primary spacing within this range is history-dependent [20, 25, 32, 45, 46, 51, 53-57]. In a typical Bridgman experiment where the pulling velocity

V_p of the sample is suddenly increased, the initial wavelength of morphological instability λ_i during the transient recoil of the interface, from a planar front at rest, is typically much smaller than the final dynamically selected primary spacing. Since disordered dendritic hexagonal arrays are generally formed in three-dimensional (3D), this history-dependent spacing is not unique and exists within a dynamically selected range between a minimum and maximum spacing ($\lambda_{min} < \lambda < \lambda_{max}$) that is typically much narrower than the stable range ($\lambda_{el} < \lambda < \lambda_{br}$). Furthermore, the average spacing of the array λ_{ave}, which by definition also falls in the range $\lambda_{min} < \lambda_{ave} < \lambda_{max}$, is typically closer to λ_{el} than λ_{br} since cell/dendrite elimination is the primary mode of spacing adjustment during the transient recoil of the solidification front [52, 58].

Despite the extensive literature on directional solidification, the stability limits λ_{el} and λ_{br} of spatially extended 3D arrays have not been quantitatively characterized under diffusive growth conditions and compared to the predictions of phase field (PF) simulations that are the only current method to accurately predict those limits [58]. The main aim of the present paper is to characterize these limits experimentally by using the microgravity environment of the International Space Station (ISS) where dendritic arrays grow under purely diffusive growth conditions and to perform a quantitative comparison with PF simulations. Experimentally, we characterize the array stability limits by performing pulling velocity jumps, a method extensively used previously in thin-sample directional solidification experiments [45, 51, 59]. This makes it possible to induce dendrite elimination by a sudden decrease of pulling velocity from $V_{p,1}$ to $V_{p,2} < V_{p,1}$, which causes some of the initially dynamically selected spacings at $V_{p,1}$, which must be in the range λ_{el} ($V_{p,1}$) < λ < λ_{br} ($V_{p,1}$), to fall below λ_{el} ($V_{p,2}$). Conversely, tertiary branching can be induced by a sudden increase of velocity from $V_{p,1}$ to $V_{p,2} > V_{p,1}$, which causes some of the initially selected spacings at $V_{p,1}$ to exceed λ_{br} ($V_{p,2}$). Using this approach, we are able to characterize for the first time quantitatively the 3D array stability limits. In PF simulations, we primarily characterize the array stability limits using a computationally more efficient, albeit equivalent, method [60]. We simulate a single unit cell of a spatially periodic hexagonal array structure and determine $\lambda_{el}(V_p)$ and $\lambda_{br}(V_p)$ at fixed V_p by decreasing and increasing λ, respectively, in small steps until instability occurs. We also validate these predictions with a few velocity-jump simulations.

Real-time monitoring and observation of the growth dynamics at the interface is an essential method for understanding and characterizing the time evolution of the interface pattern. The use of transparent organic alloys has been introduced and widely acknowledged as metal analogs in solidification studies for more than 50 years [61-73]. These non-faceted organic compounds present interfacial properties very similar to those of metals. Most of the studies of directional solidification of transparent alloys, with real-time observation, were carried out on thin rectangular samples. One of their spatial dimensions, the thickness, is in the same order of magnitude as the characteristic size of the microstructures. The growth pattern is considered bidimensional. While it brings several experimental simplifications in comparison to bulk samples (absence or drastic reduction of thermosolutal convection in the liquid and better control of the thermal field), the study of the growth dynamics remains, however, limited. In three-dimensional geometries, with configurations closer to real metallurgy conditions, the thermosolutal convection in the liquid can disturb the diffusive dynamics on a range of length scales. These effects are particularly important from an industrial point of view. More fundamentally, the plethora and complexity of the dynamic phenomena to analyze is linked to the large number of degrees of freedom, in particular around the pulling axis, which allows the existence of several types of stationary microstructures of varying degrees of symmetry such as the formation of hexagonal symmetry arrangements. In fact, the main challenge in the investigation of solidification microstructure formation in 3D bulk samples stems from the thermosolutal convection in the liquid. The pattern formation is governed by the interplay between the moving solid-liquid interface and the diffusion in the liquid of chemical species and heat. In the Earth's gravity the thermosolutal gradient that forms in the liquid results in convective flow which will disturb the solidification dynamics on a large scale [74-83]. Reduced gravity conditions are necessary to investigate homogeneous microstructure growth, which has motivated solidification experiments in Space for over twenty years[83, 84].

Although a microgravity level of approximately $10^{-4}g$ is achieved in the module where experiments were performed, residual convection in the melt, while minor, can still manifest as macrosegregation. While buoyancy-driven convection is largely suppressed, other effects, such as Marangoni flows, may still contribute to fluid movements under these conditions. Previous studies have shown that a microgravity level of $10^{-6}g$ is typically required to achieve purely diffusive growth, particularly at low pulling velocities [79]. However, this threshold is less critical in our case, as the pulling velocities in experiments are sufficiently high to significantly reduce the impact of residual convection.

The experiments presented in this paper were realized in the Directional Solidification Insert (DSI) of the DECLIC instrument (DEvice for the study of Critical Liquids and Crystallization). It is installed in the International Space Station (ISS) in the framework of a collaborative project between the French and American space agencies, CNES and NASA. It is dedicated to the real-time *in-situ* observation of the interfacial microstructure during directional solidification of 3D bulk samples of transparent organic alloys. The first set of experiments (DSI campaign) was conducted in 2010-2011, focusing primarily on cellular growth using a sample of Succinonitrile (SCN)-0.24 wt% camphor, which resulted in novel observations and enhancements to the numerical models of solidification [39, 60, 85-99]. The second flight campaign, DSI-R, occurred in 2017-2018 and was exclusively dedicated to the dendritic growth by using a more concentrated alloy SCN-0.46 wt% camphor.

Modeling and simulation approaches play a pivotal role in understanding microstructural development during solidification. Computational models, ranging from cellular automata to phase-field, attempt to estimate and predict microstructural length scales based on phenomenological laws or fundamental thermodynamic concepts. In order to provide benchmark data for the simulations, the main objective of this work is to determine the stability band of dendritic patterns for a large set of pulling velocities V_p. In fact, no elimination instability nor tertiary branching was observed during long experiments with a single constant pulling velocity after the establishment of steady state, outside of sub-grain boundaries. To determine the limits, experiments with velocity jump were carried out. This paper is organized as follows. Section 2 is dedicated to the experiments, including a description of the experimental set-up and of the experiments used in this study. The results of the measurement of the DSI-R stability band are presented and discussed. Section 3 introduces the numerical phase-field simulation methods. Section 4 presents the results of the phase-field simulations and compares them to the experimental observations. These results consist of the stability band at steady-state conditions as well as the time evolution of the solidification front position and the wavelength of the initial breakdown.

2 Bulk directional solidification in microgravity

2.1 Methods

2.1.1 *DECLIC DSI Experimental Set-Up*

The DSI-R experimental campaign uses the DSI device, consisting of a vertical Bridgman furnace and a cartridge composed of a 10-mm diameter and 130-mm long quartz cylinder combined with a stainless-steel volume compensator accommodating volume changes during the phase transitions. This design enables the comprehensive study of the entire development of extended 3D patterns, ranging from the initial transient to the steady state. The difference between DSI and DSI-R campaigns lies in the use of a more concentrated alloy which allows the formation of dendritic microstructures to be studied in the ranges of temperature gradients G (12-19 K/cm) and velocities V_p (0.5-12 µm/s). The cartridge was vacuum filled (0.1 mbar) with a succinonitrile (SCN)-0.46 wt% camphor alloy. The SCN used was purified at NASA/MSFC through distillation and zone melting and characterized for purity in a vacuum sealed glass ampoule that was delivered to the experimental team members at Iowa State University, Northeastern University and IM2NP. The camphor for the flight experiment was sublimated three times at the IM2NP laboratory. The final step of the on-ground sample preparation consisted in the formation of a monocrystalline seed filling the whole crucible with a <100> direction parallel to the pulling axis. Further details about the experimental procedure are given in [100]. On board the ISS, the solidification experiments are performed by pulling the cartridge inside the thermal gradient at a constant pulling velocity for the whole solidification length or at varying pulling velocities. The apparatus allows the observation of the solid-liquid interface through three distinct optical modes, illustrated in Fig. 1. The main observation mode is the top-view (axial) observation, as shown in Fig. 1-top. In this configuration, the crucible is illuminated from the bottom by a light-emitting diode (LED), and the interface is observed from the top thanks to a CCD camera. On the same axis, a He-Ne laser interferometer is also available for reconstructing the dendrite tip morphology in 3D over a depth of several hundred micrometers (Fig. 1-bottom). In addition to that, a transverse observation mode provides side-view imaging of the interface motion and macroscopic shape (Fig. 1-middle).

In the DSI-R flight experiments, *in-situ* real time observation of one complete experiment generates approximately ten thousand grey-scale images of the solid-liquid interface. Extracting the rich information contained in the image sequences requires in-depth analysis using automated image processing methods. In this study, only top-view observation of the pattern was used and discussed. Several semi-automatic procedures were developed by our team and the details can be found in [100]. The growth direction of dendrites is mainly determined by the crystal orientation, and they predominately grow along <100> in succinonitrile due to its body centered cubic (BCC) crystal structure. Brightness variations in the 2D pattern result from parts of the tip surface that are more aligned with the optical axis appearing brighter, while the grooves between dendrites, situated farther from the optical axis, appear darker.

To sum up the image processing procedures, we generate a binary mask on each axial image wherein each dendrite is individually detected and identified, enabling the calculation of the center for each dendrite. Subsequently, a Voronoi tessellation of these identified centers is employed to determine the first neighbors of each dendrite at a specific time and compute its primary spacing, represented by the average center-to-center distance with first-neighbor dendrites in top-view images. A complete description of these procedure can be found in [100].

2.1.2 Velocity jump experiments

As described in [58], each experiment starting from rest using a fixed pulling velocity develops a unique primary spacing distribution. But the dynamical selection of this distribution is history-dependent so that it can be modified using different initial conditions. To establish the stability limits at each reference velocity a series of “unitary velocity jump” experiments were then performed. This method is designed to expose these different initial states to the limits of primary spacing stability. Stability limits are generally characterized by a tertiary branching instability at large spacing (λ_{br}) and an elimination instability at small λ values (λ_{el}) and the goal of exposing these different initial states is to explore the dynamic adjustment in spacing to a specific reference velocity.

In this paper, we will mainly focus on one long experiment at a constant pulling rate of V_p = 3 µm/s for the whole experiment and four experiments with a single pulling velocity jump performed in the middle of the solidification run under a thermal gradient of G = 12 K/cm. Each experiment starts at an initial velocity, $V_{p,1}$, which then increases or decreases to $V_{p,2}$ = 3 µm/s. The main steps of these experiments are schematized in Fig. 2a. Initially, the cartridge is positioned in the thermal gradient such that the majority of the sample is liquid. At rest (V_p = 0 µm/s; t = 0 s; pulled length L = 0 mm), the solid-liquid interface is smooth and convex; after imposing the first velocity, $V_{p,1}$, the interface starts to destabilize. The dynamic breakdown is very fast and quickly forms a complex disordered dendritic pattern until slowly reaching a more ordered steady state (Fig. 2b-i). Generally, $V_{p,1}$ is applied for 30 mm of solidification after which the pulling velocity is modified to $V_{p,2}$. The dendrites morphology quickly evolves (Fig. 2b-ii and iii) and solidifies for another 30 mm (Fig. 2b-iv)). Although the analysis methodology is only detailed for V_p = 3 µm/s, similar analyses have also been performed for other velocities ranging from 0.75 to 12 µm/s to determine instabilities thresholds.

The pulling velocity of 3 µm/s represents a "reference" experiment as the solid-liquid interface is macroscopically flat during steady-state growth, with therefore minimal curvature influence on primary spacing evolution [58]. The macroscopic solidification front curvature depends on the pulling velocity [58, 60]: the front becomes less convex, where dendrite tips are more advanced in the middle of the sample than the edges, as pulling velocity increases to reach a macroscopically flat shape at V_p = 3 µm/s. It then becomes more and more concave in the solidification direction as pulling velocity increases. The curvature prevents the pattern from achieving a stationary state, leading to a continuous increase of the primary spacing in the convex case and continuous decrease in the concave one, resulting from the formation of a drift velocity gradient inwards or outwards the center of the interface driven by an interplay between crystal misorientation and interface curvature [58]. At V_p = 3 µm/s, the average spacing stabilizes after the initial transient stage. An image of the dendritic pattern at steady state can be seen in Fig. 2c. Four pulling rates, $V_{p,1}$, were selected: 0.75, 1.5, 6 and 12 µm/s. The objective is to study the selection of primary spacing, which includes examining the history dependence and stability limits of primary spacing. The different experiments are designated by: *A* (from 0.75 to 3 µm/s); *B* (from 1.5 to 3 µm/s); *C* (from 6 to 3 µm/s); *D* (from 12 to 3 µm/s).

2.2 Primary spacing evolution and selection

The long experiment at 3 µm/s with no velocity jump, presents a flat solid-liquid interface. Measurements of the spacing across the interface over time define the dynamic spacing selection, specific to this experiment, with a dynamically selected maximum λ_{max} = 630 µm, minimum λ_{min} = 320 µm, and average spacing λ_{ave} = 490 µm [58] (Fig. 4e). Since no elimination nor tertiary branching instability could be observed, these values are within the stability band but do not define its limits.

Figure 3 displays the evolution of the pattern and the primary spacing maps associated to four critical steps of the solidification process in experiment *A*: after the initial transient (a), just before (b) and after (c) the jump and at the end of solidification (d). In this case, the interface features only one well oriented grain. For dendrites on the crucible border, the primary spacing is poorly defined due to the absence of first neighbors and is characterized on the spacing map by large domains which are ignored during the analysis. Figure 4 shows the evolution of the dynamically selected minimum λ_{min}, average λ_{ave}, and maximum λ_{max} spacing for the four experiments *A* to *D* along the whole solidification process. The minimum and maximum spacing displayed in Fig. 4 are, at each moment, the extreme values of the spacing measured on the whole interface.

The initial pattern at $V_{p,1}$ = 0.75 µm/s presents poorly branched dendrites, close to cellular microstructures (Fig. 3a), with a spacing distribution ranging from 400 to 600 µm (Fig. 4a). The dendrite branches develop slowly and in accordance with previous results [58], under the influence of the convex interface, the dendrites stretch and lead to a continuous increase in time of the spacing. As shown in Fig. 3b, after 29.6 mm of solidification, the spacing ranges from approximately λ_{min} = 600 µm to λ_{max} = 850 µm. Immediately after the pulling velocity jump, at $V_{p,2}$ = 3 µm/s (Fig. 3c), the dendrites morphology evolves with the thinning of the dendrite trunk and the emergence of well-defined secondary branches developing in the space between each dendrite all at the same orientation as expected. However, the spacing distribution remains nearly identical along the whole solidification length (30 mm; 2.7 hours) with a slight decrease of about 50 µm on the whole interface (Fig. 3d).

At the start of each experiment, the primary spacing falls within a range of about 200 µm. The values of λ_{max}, λ_{ave} and λ_{min} at the start and end of each pulling velocity stage are detailed in Table 1. For all experiments, they evolve continuously and simultaneously depending on the solidification front curvature during the first stage of velocity, as explained earlier. Just after the velocity jump towards 3 µm/s, the average spacing λ_{ave} ranges from 300 µm in experiment *D* to 700 µm in experiment *A*. Although the front turns flat during the pulling stage at 3 µm/s, experiments *A* and *B* showcase a slight continuous decrease in spacing of about 50 µm along 30 mm of solidification. This effect might be linked to a very slight drift velocity gradient along the drift direction that we could not quantify [97].

In a previous study [58], it was shown that at high pulling velocities, a concave curvature of the solidification front leads to the formation of stray grains at the border of the sample. These stray grains are misoriented with respect to the pulling axis and may invade the center of the sample. This is also observed in the pulling velocity jumps coming from high velocities (experiments *C* and *D*), and the spacing measurements were therefore carried out on the central grain, which is the best oriented. The well-developed dendritic microstructure is measured after 15 mm of solidification. Experiment *C* shows the case where the velocity jump (from 6 to 3 µm/s) corresponds to the transition from a concave to a flat front. The primary spacing decreases before the jump, from (λ_{min}, λ_{ave}, λ_{max}) = (297, 391, 502) µm to (246, 370, 484) µm. The observed spacing range at $V_{p,2}$ = 3 µm/s stabilizes around these values during the remaining solidification thus assessing the stability of this spacing range at 3 µm/s.

Figure 4 details the primary spacing range evolution for experiment *D*. In this case, the alloy was solidified at 12 µm/s for 20 mm followed by 40 mm at 3 µm/s. A slight decrease in the spacing values is observed during the first solidification stage due to the influence of the concave curvature and reaches a spacing distribution between λ_{min} = 226 µm and λ_{max} = 423 µm. After the velocity jump, we noticed an increase in the minimal (229 µm) and average (339 µm) spacings followed by a stabilization at λ_{min} = 318 µm and λ_{ave} = 373 µm, while the maximal value of spacing remains the same for the entire length. Several elimination events were detected at the velocity jump allowing the adjustment of the spacing at 3 µm/s. This indicates that λ_{min} measured just after the jump to 3 µm/s, as well as the λ_{min} established between successive eliminations do not fall in the primary spacing stability band.

The variation in dendrite morphology at 3 µm/s, as shown in Fig. 4, highlights the significant role of primary spacing in shaping dendritic growth. Larger primary spacings result in more developed side branches, demonstrating the system's ability to adapt its growth pattern to the available space. This adaptability underscores how dendritic growth mechanisms dynamically respond to local conditions, optimizing the morphology based on spatial constraints. Following a velocity jump, more widely spaced dendrites consistently develop more elaborate branches at the same growth velocity, emphasizing the critical influence of initial spacing on branching dynamics. This evidence strongly supports the hypothesis that spacing drives the development of branches rather than the reverse as observed in 2D geometry [45, 101], highlighting the importance of spatial factors in understanding and predicting dendritic growth behavior under varying conditions. We can nonetheless specify that, under non-steady-state conditions—such as during the initial transient [102] or during growth driven by tertiary branching, for instance, at a grain boundary [103]—the growth dynamics of secondary branches can, in turn, influence the selected spacing but this is outside of the scope of our study here.

2.3 Upper and lower threshold determination

2.3.1 Elimination of primary dendrite arms

Figure 5 shows the evolution of the pattern, primary spacing maps and histograms for the experiment *D* (from 12 to 3 µm/s). The quite large average spacing before the velocity jump is associated to the well-developed sidebranches of dendrites (Fig. 5a). In this experiment, successive eliminations were observed right after the velocity jump (red crosses on Fig. 5b), which enabled the pattern primary spacing to return to its stability band as explained previously. Initial λ_{min} inherited from $V_{p,1}$ =12 µm/s is smaller than λ_{el} for 3 µm/s right after the velocity jump. Successive eliminations indicate that these metastable spacings are outside the stability band.

In fact, the spacing measurements for eliminated dendrites at this stage have a substantial dispersion ranging from very low spacings, far from the elimination threshold, to higher spacing close to it. As the eliminations progress and the average spacing increases, the measurements become scarcer and closer to the “real” elimination threshold λ_{el}. The resulting pattern presents then a stable, low, minimum primary spacing around 300 µm (Fig. 5c). Consequently, the “real” elimination threshold could be efficiently measured well after the velocity jump, during the stationary regime on a fairly well-ordered pattern. Moreover, measurements are performed in the middle of the central grain, far from the influence of sub-grain boundaries and from the growth competition.

In experiments *C* and *D*, more than ten events meeting these conditions were determined and analyzed. Figure 6 shows a sequence of elimination of a dendrite, surrounded by its neighbors, over time at 3 µm/s in experiment *C*. The evolution of the distance between the dendrite and each of its neighbors as well as the average distance are noted in Fig. 6. The delicate step in determining the threshold lies essentially in identifying the exact time at which the instability begins and the relevant distance to consider. To pinpoint the onset of elimination, we track the evolution of the spacing between a dendrite and its neighbors for a dendrite that is about to be eliminated, prior to the full manifestation of the instability. The onset is identified as the moment where a sharper decline in spacing is observed relative to others, as illustrated in Fig. 6. Considering the minimal distance between the “soon-to-be eliminated” dendrite and its neighbors rather than the average spacing seems to be more consistent and relevant. It was measured at 287 µm while using the average distance between each neighbor yield a threshold λ_{el} around 323 µm.

The same measurements were also realized for eliminated dendrites at sub-grain boundaries between the main central grain and the sub-grains. The same conclusions and values were obtained with no significant differences. It is also important to note here that we have not considered the number and orientation/arrangement of neighbors and the influence of interaction between secondary arms.

2.3.2 Tertiary branching resulting in new primary dendrite arms

Tertiary branches emerge from a secondary dendrite arm when there is enough space. Measuring the tertiary branching spacing threshold λ_{br} requires a fine analysis of the secondary arms growth direction. In a disordered three-dimensional pattern, such measurement poses significantly more challenges than in a two-dimensional context, especially considering that tertiary branches emerge from a secondary branch of an existing dendrite. To accurately characterize this threshold, it is crucial to consider the pattern geometry. This involves focusing on the nearest neighbor distances along the secondary branches' direction, rather than relying on the primary spacing, which calculates the average distance between neighboring dendrites.

In all experiments, only one occurrence of tertiary branching due to a large primary spacing in the central grain was observed. It corresponds unequivocally to the upper limit of the accessible range of primary spacing at 3 µm/s, observed in experiment *A*, right after the velocity jump from 0.75 to 3 µm/s. Figure 7 shows the formation of the new dendrite emerging from a secondary branch belonging to the dendrite with highest average primary spacing (826 µm); such measurement based on average spacing for tertiary branching is referred as $\lambda_{br,Ave}$. However, in general, only the distances between neighboring dendrites in the local region that are closest to where the tertiary branch emerges are relevant to calculating the branching threshold λ_{br}. This is because the growth rate of this tertiary branch is controlled by its diffusive interaction with the secondary arms of adjacent primary dendrites. In Fig. 7, these distances are labeled as λ' and λ", which yields λ_{br} = (λ'+ λ")/2 = 841 µm that is slightly larger than $\lambda_{br,Ave}$, and the location of the tertiary branching event is marked as a red cross.

Other occurrences of tertiary branching were also observed at sub-grain boundaries and yield approximately the same threshold. Figure 8 shows a tertiary branching event at 3 µm/s in experiment *D* at a sub-grain boundary. The sub-grains G1 and G2, as defined in the Fig. 8, are slightly misoriented ($\Delta\theta$ = 3°) with G2 exhibiting a 5° misorientation angle with respect to the pulling axis. We recall that in a flat front configuration, a grain misoriented by an angle θ with respect to the pulling axis **z** causes its structures to drift along the interface at a drifting velocity V_d verifying the relation $V_d = V_p \tan(\theta)$ [78]. This implies, in this case, a drift velocity V_d difference between them ($V_d(G1)$ = 150 nm/s and $V_d(G2)$ = 240 nm/s). Since G2 drifts slightly faster than G1, the sub-boundary is diverging and the distance (or spacing λ) between the two dendrites considered in Fig. 8 increase continuously with time at a velocity of 90 nm/s ($V_d(G2) - V_d(G1)$). Moreover, the drift direction is, in this case, parallel to the direction of secondary arms growth. This configuration can be considered as analogous to a thin-sample geometry growth as schematized in Fig. 8d. The distance $\delta = [V_d\ (G2) - V_d\ (G1)]\Delta t$ increases with time and a new dendrite, i.e. tertiary branching here belonging to grain G2, is detected when the spacing λ reaches about 821 µm. This value corresponds to the branching threshold value λ_{br} and coincides well with the previous measurement inside the central grain far from sub-boundaries. The local spacing λ of the newly formed dendrite sits at 455 µm. This observation allows us to be confident in the measurement of instability threshold values on experiments with or without velocity jumps on tertiary branching taking place in the central grain or at grain boundaries for any velocity.

More generally, the relationship between spacing, branching, and pattern organization in dendritic growth appears to be case-dependent, making it challenging to establish a universal criterion for measuring branching thresholds. However, our observations reveal a remarkable consistency in tertiary branching thresholds between the central grain and grain boundaries, despite the latter exhibiting more variation in pattern organization and neighbor distribution. This consistency holds as long as the analysis focuses on the nearest neighbors oriented along the direction of the secondary arm leading to the formation of the new dendrite. In our experiments, pattern organization does not appear to influence the tertiary branching threshold itself, even if it may affect the evolution of spacing dynamics.

2.3.3 DSI-R stability band

Figure 9 shows the primary spacing accessibility bands at 3 µm/s as a function of the initial velocity $V_{p,1}$. In black, the accessibility band of a reference experiment at 3 µm/s shown over the entire solidification length, i.e. without any pulling velocity jump, is given. The stability band could be bounded at large spacing values by the maximum accessible value λ_{max} in experiment *A*, which corresponds to the branching instability threshold, λ_{br} = 841 µm, and bounded at small values by λ_{min} in experiment *D*, which corresponds to the elimination instability threshold, λ_{el} = 284 µm. Therefore, we have unequivocally determined the stability range at 3 µm/s for our system.

One can notice that at V_p = 3 µm/s, where the solidification front remains flat, the system retains the spacing distribution of the initial state, dictated by the final distribution at $V_{p,1}$ before the jump. This explains why spacing values in constant velocity experiments deviate from those observed under velocity jump conditions or other experimental setups. The lack of imposed initial conditions in constant velocity cases inherently ties the variability to the system's prior state. However, a general trend of decreasing primary, maximum, and minimum spacings following a power law, as expected, is still observed. In this context, the spacing band at 3µm/s after the velocity jump from 1.5 µm/s appears to deviate from this trend, with a significant reduction in the spacing compared to the jump from 0.75 µm/s. This discrepancy can be understood by considering the role of interface curvature. At 0.75 µm/s the strong curvature significantly increases the spacing continuously, resulting in a more pronounced preselected distribution. At 1.5 µm/s, the curvature effect is less pronounced and has not yet reached a comparable state. If the system had been allowed to stabilize longer at 1.5 µm/s, the spacing would likely have increased further, leading to a broader spacing band at 3 µm/s. This highlights the importance of curvature in influencing the dynamics of spacing selection and emphasizes the transient nature of preselected distributions following velocity jumps.

Figure 10 exhibits the stability bands obtained at several velocities (from 0.75 to 12 µm/s) for each type of instability (elimination and tertiary branching). Two methods were used: the first using the average distance to neighbors ($\lambda_{\text{el-average}}$ and $\lambda_{\text{br-average}}$), and the other, more relevant, considering the geometry of the arrangement as explained above and measured manually (λ_{el} and λ_{br}). For each velocity, the values represented correspond to the average of all occurrences. The values considered and presented come from measurements taken across in the main grain, sub-grains or at sub-boundaries, for long experiments at constant pulling velocity and experiments with velocity jumps. Every occurrence of tertiary branching and elimination were considered in the ten or so experiments analyzed. At 1.5 and 2 µm/s, no branching event was observed, while at 0.75 µm/s no elimination could be detected. This is why the respective rectangles are not closed. The results show a large band of stability at all velocities. As expected, the upper limit of spacing stability, i.e. the branching threshold, decreases with increasing velocity. However, the measurements show a relatively close lower limit of the spacing stability band at all velocities: it ranges from 250 µm at 12 µm/s to 321 µm at 1.5 µm/s. Table 2 provides a summary of the observed elimination and branching instabilities across a range of velocities for all experimental conditions, including both velocity jumps and constant velocity scenarios. The table details the number of occurrences and the specific locations where these instabilities were recorded, notably within the central grain and along sub-grain boundaries, with the highest frequency observed at the sub-grain boundaries.

At sub-grain boundaries, shifts in velocity alter the macroscopic curvature of the solidification front. This curvature change alters the local growth direction V_g with respect to the thermal axis and hence the pattern drift velocity V_d in two adjacent grains of different misorientations (see Ref. [58]). Thus, when a velocity jump modifies the curvature, it reshapes the geometric configuration, potentially accentuating the divergence of a sub-grain boundary and triggering tertiary branching depending on the relative orientation of the two grains. Although interface curvature influences the spatial distribution and behavior of sub-grain boundaries, its role, in our examples, is secondary to the dominant effects of the system's intrinsic crystallography. The complexities and full implications of these curvature-induced changes will be further explored in future studies.

The observed thresholds for instabilities, particularly elimination and tertiary branching, reveal clear differences depending on the measurement criteria employed. While the discrepancy for elimination thresholds ($\lambda_{\text{el-average}}$ and λ_{el}) remains within 10%, differences for tertiary branching thresholds ($\lambda_{\text{br-average}}$ and λ_{br}) can reach up to 35%, such as at 12 µm/s. Using our defined measurement criterion, the calculated ratios of $\lambda_{br}/\lambda_{el}$, which describe the width of the stability band, consistently range between 3 and 4. It is important to emphasize that no other direct experimental measurements of 3D stability thresholds currently exist, as real-time monitoring is essential for capturing these dynamics, which are difficult to access through *post-mortem* analyses in metallic systems. The use of advanced tools, such as dynamic tracking at grain boundaries and velocity jump methods, has proven to be highly effective for probing the spacing instabilities, highlighting their potential for further exploration in 3D studies. This lack of direct comparison underscores the significance of our results, as they provide some of the first benchmarks for 3D stability thresholds.

Nonetheless, prior experimental and numerical studies, both in 2D [25, 54, 104] and 3D [39, 105, 106], have highlighted the impact of dimensionality on stability bands and spacing selection. Experimental 2D systems typically exhibit narrower stability band ratios closer to 2 [47, 101]. In contrast, our 3D results demonstrate broader bands, reflecting the increased flexibility and complexity inherent to 3D systems. These findings reinforce the necessity of conducting 3D benchmarks to refine models and better account for the physical dynamics of systems more representative of industrial conditions.

Recent 3D phase-field studies have further illuminated the role of the thermal gradient *G* on stability band width [57]. For low gradients, theoretical ratios as high as 5 or 6 have been reported, but as the gradient increases and approaches the cellular regime, the theoretical ratio of 2 becomes more realistic. Future studies, particularly on the effects of *G*, the dendritic-to-cellular transition, and dynamic tracking of grain boundary evolution, represent an exciting and essential avenue for advancing the understanding of 3D dendritic growth and its stability dynamics

3 Phase-field modeling

3.1 Phase-field model equations

In addition to the bulk microgravity experiments, we probed the upper and lower limits of primary spacing with an established phase-field (PF) model that quantitatively simulates dilute binary alloy solidification [60, 90, 107]. The PF equations are given in Eqs. 1 and 2, where the phase field φ varies continuously from +1 in the solid to -1 in the liquid across a diffuse interface. A preconditioned PF defined by $\varphi = tanh\left(\psi \,/\, \sqrt{2}\right)$ is used in the simulation to enhance the numerical stability at larger grid spacings [108]. Equation 3 describes the coupling of the dimensionless supersaturation field, U, to φ with *k* as the solute partition coefficient, *c* as the solute concentration, $c_l^0 = (T_m - T_0) \,/\, |m|$ which defines the *liquidus* concentration with respect to a reference temperature, $T = T_0$; the *liquidus* slope, m; and pure solvent melting point, T_m. Length in the model is scaled by the diffuse interface length, *W*, and time by the relaxation time τ_0. The dimensionless diffusivity is $\widetilde{D} = D\tau_0 \,/\, W^2 = a_1 a_2 W \,/\, d_0$ where $a_1 = 5\sqrt{2} \,/\, 8$, $a_2 = 47 \,/\, 75$, *D* is the diffusion constant of the solute in the liquid phase, and the capillary length given by $d_0 = \Gamma \,/\, |m|(1-k)c_l^0$ with the solid-liquid interfacial energy described by the Gibbs-Thomson coefficient Γ. The model equations 1 and 2 include the thermal functions $F_1(x,t)$ and $F_2(x,t)$. The dimensionless pulling velocity and thermal length are given by $\tilde{V}_P \equiv V\tau_0/W = a_1 a_2\, V\, d_0/D\, (W/d_0)^2$ and $\tilde{l}_T \equiv l_T/W = (l_T/d_0)\, 1/(W/d_0)$ respectively, which scale *x* by the interface thickness W, and *t* by the relaxation time τ_0. The dimensional thermal length is $l_T = |m|(1-k)c_l^0/G$ with the thermal gradient *G*. The coupling factor is given by $\lambda = a_1 W \,/\, d_0$. The interface free-energy anisotropy in 3D is introduced as $\gamma(n) = \gamma_0 a_S(n) = \gamma_0(1 - 3\epsilon_4)\Bigg[1 +$

$\frac{4\epsilon_4}{1-3\epsilon_4}\frac{(\partial_x\phi)^4+(\partial_y\phi)^4+(\partial_z\phi)^4}{|\nabla\phi|^4}\Big]$ [90]. This includes the average interfacial free energy of the $\{100\}$ plane γ_0, the anisotropy strength ε_4, and the interface's normal vector $\boldsymbol{n}$.

$$F_1(x,t)a_s(n)^2\frac{\partial\psi}{\partial t} = \mathrm{a_s(n)^2}\left(\nabla^2\psi - \varphi\sqrt{2}\left|\vec{\nabla}\psi\right|^2\right) + \vec{\nabla}[\mathrm{a_s(n)^2}]\cdot\vec{\nabla}\psi + \sum_{m=x,y,z}\left[\partial_m\left(\left|\vec{\nabla}\psi\right|^2 a_s(n)\frac{\partial a_s(n)}{\partial(\partial_m\psi)}\right)\right] + \sqrt{2}[\varphi - \lambda(1-\varphi^2)F_2(x,t)] \tag{1}$$

$$(1+k-(1-k)\varphi)\frac{\partial U}{\partial t} = \tilde{D}\vec{\nabla}\cdot\left[(1-\varphi)\vec{\nabla}U\right] + \vec{\nabla}\cdot\left[(1+(1-k)U)\frac{(1-\varphi^2)}{2}\frac{\partial\psi}{\partial t}\frac{\vec{\nabla}\psi}{\left|\vec{\nabla}\psi\right|}\right] + [1+(1-k)U]\frac{(1-\varphi^2)}{\sqrt{2}}\frac{\partial\psi}{\partial t} \tag{2}$$

$$U = \frac{1}{1-k}\left[\frac{c\ /\ c_l^0}{(1-\varphi)/2 + k(1+\varphi)\ /\ 2} - 1\right] \tag{3}$$

3.2 Phase-field model implementation

The phase-field equations, Eqs. 1 and 2, are solved on a cubic grid with a finite-difference discretization of spatial derivatives and a forward explicit Euler method in time. The grid spacing and time step are denoted with Δx and Δt respectively. Here we use $\Delta x/W = 1.2$ and Δt varies based on the values of W and of V to satisfy the conditions for numerical stability. The spatial discretization uses a standard seven-point stencil on a cubic lattice in 3D, involving the origin point and its six nearest-neighbor points in the ⟨100⟩ directions [109]. The PF model is solved through implementation in the computer unified device architecture (CUDA) programming language running on massively parallel graphic processing units (GPUs).

The conditions of DECLIC DSI-R experiment were simulated with the PF model. The model simulates a SCN-0.46wt% camphor alloy with G = 12.5 K/cm, k = 0.1, m = -1.365 K/wt%, D = 270 µm^2/s, ε_4 = 0.011, and Γ = 6.478·10^{-2} K-µm [98]. The pulling velocities V_p simulated include 1.5, 3, 6, and 12 µm/s. Each of these velocities are run with their own interface thicknesses to ensure each of the simulations is converged. All of the simulation parameters that vary between simulations, including interface thickness, defined as W/d_0, can be found in Table 3. The domain of the simulation in the growth direction L_x is chosen such that the liquid part L_x^{liq} is greater than five characteristic diffusion lengths, $L_x^{liq} \geq 5\left(D\ /\ V_p\right) = 5l_D$. To incorporate the effect of thermal fluctuations, we introduce noise by adding a random perturbation to the preconditioned phase-field evolution equation with a strength F = 0.02 [60, 92, 110]. Since initial linear perturbations of the interface grow exponentially fast in time, the time of onset of morphological instability and the initial wavelength only have a very weak logarithmic dependence on the noise magnitude that can be neglected.

The symmetry of the fourfold anisotropy allows us to constrain our model to one quarter of a single dendrite for more efficient simulations. For steady-state dendrites, the frozen temperature approximation (FTA) where $F_1(x,t) = 1 - (1-k)\left(x - \tilde{V}_P t\right)/\tilde{l}_T$ and $F_2(x,t) = U + \left(x - \tilde{V}_P t\right)/\tilde{l}_T$ is used for the thermal functions. To probe the upper limit of primary spacing linked to tertiary branching instability, the simulation bounds in L_y and L_z were periodically expanded using bilinear interpolation from the previous simulation to fit the new bounds until the dendrite adjusted to a lower primary spacing through tertiary branch overgrowth. Additionally, we constrained our bounds to be $L_y/L_z = \sqrt{3}/2$ to simulate dendrites packed in a hexagonal array [97]. The hexagonal packing also requires an anti-symmetric boundary condition along $z = L_z$, and we imposed a no-flux boundary along $y = L_y, y = 0$, and $z = 0$. In a hexagonal array each dendrite is surrounded by six nearest neighbors as in Fig. 11. The elimination threshold is determined from simulations of two full dendrites with domains that are successively decreased until one of the tips is eliminated [107]. Additionally, simulation results indicate that the effect of array structure on the stable spacing range is small.

The dynamically selected spacings were measured from the primary spacing resulting from the process of interface breakdown and development within a three dimensional, spatially extended simulation domain where $L_y = L_z = 1200\ \mu m$ for each velocity [60]. For this simulation, the release of latent heat and diffusion of heat was important to the evolution of the solidification front position within the thermal gradient. A one-dimensional thermal field calculation (1D TFC) was calculated with thermal functions $F_1(x,t) = 1 - (1-k)\,(T(x,t) - T_0)/\Delta T_0$ and $F_2(x,t) = U + (T(x,t) - T_0)/\Delta T_0$. The temperature field evolution in time is $\partial_t T = V\partial_x T + D_T \partial_{xx} T + \frac{\Delta h_f}{c_p}\frac{1}{\mathcal{V}}\int \frac{\dot{\varphi}}{2}\, d\mathcal{V}$ where D_T is the thermal diffusivity, Δh_f is the latent heat of fusion per unit volume, and c_p is the heat capacity, and solved similarly to the phase and solute fields with finite differences and explicit Euler time stepping. The time step in the thermal field is identical to that used to solve the phase and solute fields. With diffusivities differing by orders of magnitude, the thermal field is calculated with a rougher grid spacing, Δx_T, where the relationship between the two different grid sizes is $\Delta x_T = 24\Delta x$. The volume, $\mathcal{V}$, numerically integrated over is $\mathcal{V} = \Delta x_T \times L_y \times L_z$. The effective thermal diffusivity inside the DSI-R crucible is $D_T = 3.09 \times 10^{-7}\ m^2\ /\ s$ previously calculated by Song et al. [60].

4 Phase Field comparison to bulk microgravity experiments

4.1 Transient interface dynamics and onset of morphological instability

At the beginning of each experiment (or simulation), the planar solid-liquid interface is located close to the *liquidus* temperature of the alloy within a temperature gradient *G*. When pulling the sample, the interface recoils within the temperature frame, and the solute concentration increases on the liquid side of the interface as a solute layer builds up ahead of the interface. The planar front then undergoes the Mullins-Sekerka instability and breaks down [111]. The onset of planar instability occurs when the solute concentration gradient in front of the interface exceeds a critical value [112]. The resulting microstructures then compete with one another until they reach a stable spacing.

Experimental measurements of the time evolution of the interface position z_i starting from rest ($z_i = 0$) are shown for different V_p in Fig. 12a-d (black squares) and compared to PF simulations using the thermal field calculation (red thick solid lines)[60]. In all cases, the solid-liquid interface initially moves towards colder temperature ($z_i < 0$) because the pulling velocity is faster than the interface growth velocity. For both experiments and simulations, a local maximum appears because after the destabilization of the planar interface, small dendrites move very fast towards the hotter temperature. Then, primary dendrites approach a stationary temperature. Concerning the interface motion, there is very good agreement between experiments and simulations for V_p = 3 µm/s, where the interface of the DSI-R experiments matches the macroscopically flat interface in PF simulations

One should notice a very good agreement, no matter the pulling velocity, in the timing of the local maximum (onset of morphological instability). Figure 13a shows initial average spacings measured at the onset of instability for different pulling velocities. Figures 13b and 13c show examples of top views of the solid-liquid interface at the time of the initial breakdown in experiment and PF simulations, respectively. The initial spacing λ_0 decreases as the pulling velocity increases in both experiments and PF simulations but is larger in experiments than in simulations. Error bars correspond to standard deviations in experiments and simulations.

Discrepancies in the interface dynamics between experiments and simulations are closely linked to the effect of front curvature, particularly during the transition to steady-state growth. During the recoil phase, across all pulling velocities, there is excellent agreement between experimental and simulated front positions. At rest, at the very beginning, and throughout the recoil phase, the front remains slightly convex regardless of the pulling velocity [93]. However, as the system approaches steady-state, the curvature becomes more pronounced: the interface remains convex for pulling velocities below 3 µm/s and becomes concave for velocities above 3 µm/s. It is precisely during this phase, when the curvature is most significant, that the largest discrepancies between experiments and simulations occur.

These discrepancies, particularly for curved solidification fronts, may also arise from how the front shape is determined in experiments. For convex fronts (Fig. 1), the positions of the left, right, and center can be easily determined, and these correspond to the tip positions. For concave fronts, however, the tip positions in the center are obscured by microstructures at the crucible borders, making accurate determination impossible. The interface is often approximated as a symmetry-based curve, which, while practical, does not correspond precisely to the actual tip positions, which remain out of reach due to experimental constraints. Such approximations introduce uncertainties in capturing the exact interface dynamics. Despite these limitations, the overall agreement between experiments and simulations remains strong for pulling velocities where the front is macroscopically flat, as demonstrated by the very good match observed at V_p = 3 µm/s

This strongly suggests that curvature effects are the primary source of these deviations. At higher and lower pulling velocities, the pronounced curvature influences solute redistribution and interface dynamics in ways that are not fully captured by the models, leading to discrepancies. These findings highlight the importance of accurately accounting for curvature in simulations to improve alignment with experimental observations during steady-state growth. Additionally, the initial curvature of the solidification front influences how solute redistribution and instability develop, further complicating direct comparisons between experimental and simulated results. Despite these challenges, the trend of decreasing λ_0 with increasing pulling velocity is consistent between experiments and simulations, demonstrating that while there are discrepancies in magnitude, the underlying physics governing initial wavelength selection is well-represented in the models.

4.2 Phase-field primary spacings and comparison to bulk microgravity experiments

The results of the quarter dendrite PF simulations used to determine the tertiary branch threshold of bulk succinonitrile-0.46wt% camphor dendrites are shown in Fig. 14. The full dendrites shown in this figure reflect the symmetry of the quarter dendrite simulation. The primary spacing reported will be measured by $\lambda = 2L_y$ only. Ideally the imposed hexagonal spacing makes the local primary spacing of the six nearest neighbors equivalent to the distance between the tips found on the y-axis, but when implementing the phase field equations, the spatial discretization combined with the interface thickness may make the primary spacing of the nearest neighbor 60 degrees off the y-axis, Fig. 11, larger by a few microns.

The band of stable spacings, λ_{el} and λ_{br}, along with the dynamically selected spacings, λ_{min}, λ_{ave}, and λ_{max}, are shown in Fig. 15. To ensure that the tertiary branching threshold identified via progressive boundary expansion is equivalent to a velocity jump tertiary branching threshold, spatially extended simulations were performed with velocity jumps. The largest selected spacing found at 1.5 μm/s in Fig. 15 is only larger than the branching threshold at 12 μm/s. For PF simulations, a jump in velocity of this magnitude (1.5 to 12 μm/s) is not feasible because values of W/d_0 used in simulations at 1.5 μm/s are not converged, and spatially extend simulations of 1.5 μm/s using convergence values of 12 μm/s are too computationally intensive. Therefore, to observe the tertiary branching threshold an additional simulation was performed at 0.75 μm/s. We use the resulting steady-state microstructure of 0.75 μm/s as the initial condition for new simulations of 1.5 and 3 μm/s, separately, to simulate the velocity jumps.

A pulling velocity of 0.75 μm/s gave a selected spacing of $\sim$ 500 μm, a value below the λ_{br} threshold at 1.5 μm/s but above the threshold at 3 μm/s. Based on the measured tertiary branching thresholds, we expected the initial spacing at 0.75 μm/s would be maintained after a jump to 1.5 μm/s, and at 3 μm/s we would see primary spacing adjustment caused by tertiary overgrowth. This is exactly what we see from the simulations (see PF videos in supplementary materials) with the primary spacing adjusting to approximately half the original spacing at 3 μm/s only. We interpret these results to mean that the dynamics of the tertiary overgrowth are properly captured through boundary expansion.

Results from PF simulations qualitatively explains why we did not see dramatic primary spacing adjustments in the DSI-R experiments. The tertiary threshold observed is well above any of the selected spacings. In fact, most observed tertiary branching instabilities occurred on a sub-grain boundary (Table 2), which demonstrates that the difference in growth angle between sub-grains described in Fig. 8 was critical in measuring the experimental tertiary threshold. The only experiment where we observed tertiary overgrowth in the main grain was during a velocity jump from 0.75 to 3 μm/s, which again qualitatively matches the results from simulations.

The predicted range of stable primary spacings is compared to the observed stability bands in Fig. 16. The predicted thresholds λ_{el} and λ_{br} are shown to be approximately half of the observed average thresholds $\lambda_{el,\ Ave.}$ and $\lambda_{br,\ Ave.}$ (as defined in Fig. 10). Further, the minimum observed spacing falls squarely within the predicted stability band. Clearly, there is a significant discrepancy between the simulations and the DSI-R experiments, especially with respect to λ_{br}. We have investigated different possible origins of this discrepancy including the effects of surface tension anisotropy, thermal field effects, and the role of an extraneous ternary impurity, that will be detailed in the next paragraphs.

Experimentally measured values of the magnitude of surface tension anisotropy for pure SCN [113, 114] yield a value of $\varepsilon_4 \approx 0.0055$ that is consistent with the prediction of atomistic simulations [115]. However, both experimental predictions and atomistic simulations have significant uncertainties. In addition, anisotropy can be affected by solute addition. In a previous study of oscillatory cellular patterns in a more dilute SCN-camphor alloy [98], it was found that the period of oscillation predicted by phase-field modeling best matched the experimentally measured period for a larger value of anisotropy that is about twice larger $\varepsilon_4 \approx 0.011$. This value has been used in several subsequent studies of dilute SCN-camphor alloys [95, 97] that produced reasonably good quantitative comparisons between simulations and experiments. While we used the same value $\varepsilon_4 = 0.011$ in the present study, we also performed a parametric study of the influence of surface tension anisotropy by varying ε_4 in the range 0.007-0.011. The results show that, within this range, ε_4 has a negligible effect on the stability limits of dendritic arrays, and therefore cannot resolve the large discrepancy between modeling and experiment for the maximum stable spacing λ_{br}. Using a two-parameter form of the surface tension anisotropy [115] also did not have a significant influence on λ_{br}.

In a previous comparative study of microgravity experiments and phase-field simulations for a more dilute SCN-camphor alloy, Song et al. [60] demonstrated that including the effect of latent heat rejection at the interface on the calculation of the thermal field (instead of using the standard frozen-temperature-approximation that assumes a linear temperature gradient) modestly improves the prediction of the dynamically selected primary spacing and the initial breakup wavelength. However, in both this previous study and the present study with a more concentrated SCN-camphor alloy, the incorporation of latent heat was found to have a negligible effect on the maximum stable spacing λ_{br}.

Every precaution is taken to ensure the highest possible purity of our alloy. However, during the various steps of filling the cartridge, combined with the extended duration spent in orbit, the material could have been subject to contamination or degradation. Unfortunately, there is no way to verify the state of the sample during the experiments. We have performed thin-sample experiments demonstrating that the presence of residual water on the sample glass surfaces led to a significant increase in the average primary spacing, a conclusion reached by comparing observations in samples in which residual water was or was not removed prior to filling with camphor of the same composition as in the present microgravity experiments. We further performed a quantitative phase-field modeling study of the effect of a ternary impurity on dendrite array stability. The preliminary results demonstrate that even a small amount of water contamination in the range of 0.1-0.2wt% yields a significant increase in λ_{br} as well as a 3D branching morphology in very good quantitative agreement with microgravity observations. This increase can be theoretically interpreted to result from the fact that water has a diffusion constant in liquid SCN approximately 5 times larger than camphor, which induces longer range diffusive interactions between secondary and tertiary dendrite branches that control λ_{br}. Remarkably, even a very small amount of this fast-diffusing ternary impurity suffices to significantly increase λ_{br}. These preliminary experimental and computational results support the hypothesis that residual water contamination is at the origin of the λ_{br} discrepancy between phase-field modeling SCN-camphor and the present microgravity experiments. A more detailed exposition of phase-field modeling of ternary alloy directional solidification and a quantitative comparison of simulation results with both quasi-2D thin-sample and 3D microgravity experiments will be reported in a forthcoming paper.

5 Summary and conclusion

This study provides a comprehensive investigation into the stability limits of 3D dendritic arrays during directional solidification, utilizing unique experimental data obtained in microgravity aboard the International Space Station (ISS) and phase-field simulations. Our approach, centered on the use of velocity jump experiments, allowed for a detailed characterization of the elimination and tertiary branching instabilities. By suddenly altering the pulling velocity, we induced dynamic spacing adjustments, revealing insights into the history-dependent behavior of dendritic patterns and their selection mechanisms.

We also highlighted the system’s capacity to adopt vastly different morphologies under identical solidification conditions is particularly remarkable. Even when key parameters are held constant, dendritic growth can range from stable, simpler forms to more complex structures involving developed secondary branching. This suggests that spatial constraints or other influencing factors can favor the suppression of secondary branching. Such morphological variability can have significant effects on the final properties of the solidified material, as dendrite structure directly impacts mechanical and physical characteristics. Gaining a deeper understanding of this behavior could pave the way for enhanced control over microstructures in solidification processes, enabling the strategic manipulation of primary spacing to tailor dendrite structures for desired material performance.

The velocity jump method proved especially effective for probing the stability limits, as it exposed dendritic arrays to extreme conditions that are difficult to replicate under steady-state growth conditions. This approach not only helped us identifying the stability thresholds of elimination and tertiary branching, λ_{el} and λ_{br}, but also provided a framework for understanding how spacing evolves in response to velocity changes. Importantly, we observed that tertiary branching instabilities were frequently initiated at sub-grain boundaries, rather than within the main grains. This observation underscores the critical role of controlled sub-grain boundaries in solidification dynamics. Rather than promoting a broad and unstable spacing distribution, these sub-grain boundaries facilitated a more organized adjustment of primary spacing, highlighting their potential significance in the broader context of grain competition and pattern evolution. The impact of sub-grain boundaries and the dynamics of grain competition represent an exciting direction for future research. A separate study focused specifically on these mechanisms could further illuminate the underlying physics of solidification and provide additional insights into the role of sub-boundaries in microstructure development.

In PF simulations, λ_{br} is significantly smaller than in experiment. For this reason, it was possible to induce tertiary branching through a velocity jump that causes the dendritic array structure to leave the range of stable spacings at the new velocity, i.e. for a velocity jump from $V_{p,1}$ to $V_{p,2} > V_{p,1}$ the dynamically selected spacing at $V_{p,1}$ exceeds λ_{br} at $V_{p,2}$. Tertiary branching is not observed in experiment through a velocity jump only because λ_{br} at $V_{p,2}$ is larger than the spacings selected at $V_{p,1}$ for the range of $V_{p,2}$ investigated. The origin of the quantitative discrepancy between modeling and experiment for λ_{br} will be further analyzed in a forthcoming paper that explores the role of water contamination.

Acknowledgments

This work was supported by CNES (French Space Agency) and by NASA (National Aeronautics and Space Administration) Grant No. 80NSSC22K0664. It is based on observations with the DECLIC-DSI (Directional Solidification Insert of the DEvice for the study of Critical LIquids and Crystallization) embarked on the ISS (International Space Station). K.J. acknowledges partial support from Lawrence Livermore National Laboratory under Contract DE-AC52-07NA27344.

6 References

[1] M.C. Flemings, Solidification processing, Metallurgical transactions 5(10) (1974) 2121-2134.
[2] R. Trivedi, W. Kurz, Dendritic growth, International Materials Reviews 39(2) (1994) 49-74.
[3] W. Kurz, M. Rappaz, R. Trivedi, Progress in modelling solidification microstructures in metals and alloys. part ii: dendrites from 2001 to 2018, International Materials Reviews 66(1) (2021) 30–76.
[4] R. Nasser-Rafi, R. Deshmukh, D.R. Poirier, Flow of interdendritic liquid and permeability in pb-20 Wt Pct Sn alloys, Metallurgical Transactions A 16(12) (1985) 2263-2271.
[5] D.R. Poirier, Permeability for flow of interdendritic liquid in columnar-dendritic alloys, Metallurgical Transactions B 18(1) (1987) 245-255.
[6] S. Ganesan, C.L. Chan, D.R. Poirier, Permeability for flow parallel to primary dendrite arms, Materials Science and Engineering: A 151(1) (1992) 97-105.

[7] C. Beckermann, Modelling of macrosegregation: Applications and future needs, International Materials Reviews 47(5) (2002) 243-261.

[8] R.G. Santos, M.M.D. Lourdes, Permeability of interdendritic channels, Materials Science and Engineering: A 391 (2005) 151–158.

[9] W. Osorio, C. Freire, A. Garcia, The effect of the dendritic microstructure on the corrosion resistance of Zn–Al alloys, Journal of Alloys and Compounds 397 (2005) 179-191.

[10] W.R. Osorio, P.R. Goulart, A. Garcia, G.A. Santos, M. Neto Carlos, Effect of dendritic arm spacing on mechanical properties and corrosion resistance of Al 9 Wt Pct Si and Zn 27 Wt Pct Al alloys, Metallurgical and Materials Transactions A 37(8) (2006) 2525-2538.

[11] W. Osorio, J. Spinelli, I. Ferreira, A. Garcia, The roles of macrosegregation and of dendritic array spacings on the electrochemical behavior of an Al-4.5 wt.% Cu alloy, Electrochimica Acta 52 (2007) 3265-3273.

[12] A.E. Ares, L.M. Gassa, S.F. Gueijman, C.E. Schvezov, Correlation between thermal parameters, structures, dendritic spacing and corrosion behavior of Zn–Al alloys with columnar to equiaxed transition, Journal of Crystal Growth 310(7) (2008) 1355-1361.

[13] T. Takaki, S. Shinji, O. Munekazu, S. Yasushi, A. Takayuki, Permeability prediction for flow normal to columnar solidification structures by large–scale simulations of phase–field and lattice Boltzmann methods, Acta Materialia 164 (2018).

[14] J.S. Langer, Instabilities and pattern formation in crystal growth, Reviews of Modern Physics 52(1) (1980) 1-28.

[15] E. Ben-Jacob, N. Goldenfeld, B.G. Kotliar, J.S. Langer, Pattern Selection in Dendritic Solidification, Physical Review Letters 53(22) (1984) 2110-2113.

[16] M. Ben Amar, E. Brener, Theory of pattern selection in three-dimensional nonaxisymmetric dendritic growth, Physical Review Letters 71(4) (1993) 589-592.

[17] E. Brener, Needle-crystal solution in three-dimensional dendritic growth, Physical Review Letters 71(22) (1993) 3653-3656.

[18] A. Karma, Y.H. Lee, M. Plapp, Three-dimensional dendrite-tip morphology at low undercooling, Physical Review E 61(4) (2000) 3996-4006.

[19] R. Trivedi, W. Kurz, Solidification microstructures: A conceptual approach, Acta Metallurgica et Materialia 42(1) (1994) 15-23.

[20] W. Kurz, D.J. Fisher, Dendrite growth at the limit of stability: tip radius and spacing, Acta Metallurgica 29(1) (1981) 11-20.

[21] J.D. Hunt, Solidification and Casting of Metals: Proceedings of an International Conference on Solidification, 1979.

[22] M.H. Burden, J.D. Hunt, Cellular and dendritic growth. II, Journal of Crystal Growth 22(2) (1974) 109-116.

[23] R. Trivedi, Theory of dendritic growth during the directional solidification of binary alloys, Journal of Crystal Growth 49(2) (1980) 219-232.

[24] R. Trivedi, Interdendritic Spacing: Part II. A Comparison of Theory and Experiment, Metallurgical Transactions A 15(6) (1984) 977-982.

[25] S.-Z. Lu, J.D. Hunt, A numerical analysis of dendritic and cellular array growth: the spacing adjustment mechanisms, Journal of Crystal Growth 123(1) (1992) 17-34.

[26] J.D. Hunt, D.G. McCartney, Numerical finite difference model for steady state cellular array growth, Acta Metallurgica 35(1) (1987) 89-99.

[27] J.D. Hunt, A numerical analysis of time dependent isolated dendritic growth for conditions near the steady state, Acta Metallurgica et Materialia 38(3) (1990) 411-418.

[28] J.D. Hunt, A numerical analysis of dendritic and cellular growth of a pure material investigating the transition from “array” to “isolated” growth, Acta metallurgica et materialia 39(9) (1991) 2117-2133.

[29] S.-Z. Lu, J.D. Hunt, P. Gilgien, W. Kurz, Cellular and dendritic growth in rapidly solidified Al-Fe and Al-Cu alloys, Acta metallurgica et materialia 42(5) (1994) 1653-1660.

[30] W. Kurz, B. Giovanola, R. Trivedi, Theory of microstructural development during rapid solidification, Acta metallurgica 34(5) (1986) 823-830.

[31] J.D. Hunt, R.W. Thomas, Microscopical modelling of binary/multicomponent alloys, pp. 350-353.

[32] J.A. Warren, J.S. Langer, Prediction of dendritic spacings in a directional-solidification experiment, Physical Review E 47(4) (1993) 2702-2712.

[33] G. Ding, W. Huang, X. Lin, Y. Zhou, Prediction of average spacing for constrained cellular/dendritic growth, Journal of crystal growth 177(3-4) (1997) 281-288.

[34] J.D. Hunt, Pattern formation in solidification, Science and Technology of Advanced Materials 2(1) (2001) 147-155.

[35] D. Ma, Modeling of primary spacing selection in dendrite arrays during directional solidification, Metallurgical and Materials Transactions B 33 (2002) 223-233.

[36] B.J. Spencer, H.E. Huppert, On the solidification of dendritic arrays: An asymptotic theory for the directional solidification of slender needle crystals, Acta materialia 45(4) (1997) 1535-1549.

[37] D. Bouchard, J.S. Kirkaldy, Scaling of intragranuiar dendritic microstructure in ingot solidification, Metallurgical and Materials Transactions B 27 (1996) 101-113.

[38] D. Ma, Response of primary dendrite spacing to varying temperature gradient during directional solidification, Metallurgical and Materials Transactions B 35 (2004) 735-742.

[39] S. Gurevich, A. Karma, M. Plapp, R. Trivedi, Phase-field study of three-dimensional steady-state growth shapes in directional solidification, Physical Review E 81(1) (2010) 011603.

[40] S. Gurevich, M. Amoorezaei, N. Provatas, Phase-field study of spacing evolution during transient growth, Physical Review E—Statistical, Nonlinear, and Soft Matter Physics 82(5) (2010) 051606.

[41] M.A. Eshelman, V. Seetharaman, R. Trivedi, Cellular spacings—I. Steady-state growth, Acta Metallurgica 36(4) (1988) 1165-1174.

[42] V. Seetharaman, M.A. Eshelman, R. Trivedi, Cellular spacings—II. Dynamical studies, Acta Metallurgica 36(4) (1988) 1175-1185.

[43] K. Somboonsuk, J.T. Mason, R. Trivedi, Interdendritic spacing: part I. Experimental studies, Metallurgical and Materials Transactions A 15 (1984) 967-975.

[44] G. Hansen, S. Liu, S. Lu, A. Hellawell, Dendritic array growth in the systems nh4cl–h2o and [ch2cn]2–h2o: steady state measurements and analysis, Journal of Crystal Growth 234(4) (2002) 731-739.

[45] K. Somboonsuk, R. Trivedi, Dynamical studies of dendritic growth, Acta Metallurgica 33(6) (1985) 1051-1060.

[46] R. Trivedi, K. Somboonsuk, Pattern formation during the directional solidification of binary systems, Acta Metallurgica 33(6) (1985) 1061-1068.

[47] S.H. Han, R. Trivedi, Primary spacing selection in directionally solidified alloys, Acta Metallurgica et Materialia 42(1) (1994) 25-41.

[48] X. Lin, W. Huang, J. Feng, T. Li, Y. Zhou, History-dependent selection of primary cellular/dendritic spacing during unidirectional solidification in aluminum alloys, Acta Materialia 47(11) (1999) 3271-3280.

[49] D.G. McCartney, J.D. Hunt, Measurements of cell and primary dendrite arm spacings in directionally solidified aluminium alloys, Acta Metallurgica 29(11) (1981) 1851-1863.

[50] J.T. Mason, J.D. Verhoeven, R. Trivedi, Primary dendrite spacing I. Experimental studies, Journal of Crystal Growth 59(3) (1982) 516-524.

[51] H. Weidong, G. Xingguo, Y. Zhou, Primary spacing selection of constrained dendritic growth, Journal of Crystal Growth 134(1) (1993) 105-115.

[52] W. Losert, B.Q. Shi, H.Z. Cummins, Evolution of dendritic patterns during alloy solidification: From the initial instability to the steady state, Proceedings of the National Academy of Sciences 95(2) (1998) 439-442.

[53] W.K. R. Trivedi, Dendritic growth, International Materials Reviews 39(2) (1994) 49-74.

[54] J.D. Hunt, S.Z. Lu, Numerical modeling of cellular/dendritic array growth: spacing and structure predictions, Metallurgical and Materials Transactions A 27(3) (1996) 611-623.

[55] W. Kurz, D.J. Fisher, Fundamentals of solidification, Trans Tech Publications, Switzerland, 4th rev. ed edition1998.

[56] J. Strickland, B. Nenchev, H. Dong, On Directional Dendritic Growth and Primary Spacing—A Review, Crystals, 2020.

[57] B. Bellón, A.K. Boukellal, T. Isensee, O.M. Wellborn, K.P. Trumble, M.J.M. Krane, M.S. Titus, D. Tourret, J. LLorca, Multiscale prediction of microstructure length scales in metallic alloy casting, Acta Materialia 207 (2021) 116686.

[58] F.L. Mota, K. Ji, L.S. Littles, R. Trivedi, A. Karma, N. Bergeon, Influence of macroscopic interface curvature on dendritic patterns during directional solidification of bulk samples: Experimental and phase-field studies, Acta Materialia 250 (2023) 118849.

[59] J. Bechhoefer, A. Libchaber, Testing shape selection in directional solidification, Physical Review B 35(3) (1987) 1393-1396.

[60] Y. Song, D. Tourret, F.L. Mota, J. Pereda, B. Billia, N. Bergeon, R. Trivedi, A. Karma, Thermal-field effects on interface dynamics and microstructure selection during alloy directional solidification, Acta Materialia 150 (2018) 139-152.

[61] K.A. Jackson, J.D. Hunt, Lamellar and rod eutectic growth, Trans. Metall. Soc. AIME 236 (1966) 1129.

[62] J.D. Hunt, K.A. Jackson, Binary eutectic solidification, Transactions of the Metallurgical Society of AIME 236(6) (1966) 843.

[63] J.D.H. K. A. Jackson, D. R. Uhlmann, and T. P. Seward, On the origin of equiaxed zone in castings, Trans. Metall. Soc. AIME 236 (1966) 149-155.

[64] K.A. Jackson, J.D. Hunt, Transparent compounds that freeze like metals, Acta Metallurgica 13(11) (1965) 1212-1215.

[65] S.C. Huang, M.E. Glicksman, Overview 12: Fundamentals of dendritic solidification—I. Steady-state tip growth, Acta Metallurgica 29 (1981) 701-715.

[66] C. Weiss, N. Bergeon, N. Mangelinck-Noël, B. Billia, Effects of the Interface Curvature and Dendrite Orientation in Directional Solidification of Bulk Transparent Alloys, Materials Science Forum - MATER SCI FORUM 508 (2006) 337-342.

[67] S. Bottin-Rousseau, M. Perrut, C. Picard, S. Akamatsu, F. Gabriel, An experimental method for the in situ observation of eutectic growth patterns in bulk samples of transparent alloys, Journal of Crystal Growth 306(2) (2007) 465-472.

[68] N. Bergeon, C. Weiss, N. Mangelinck-Noël, B. Billia, Interferometric method for the analysis of dendrite growth and shape in 3D extended patterns in transparent alloys, Transactions of the Indian Institute of Metals 62(4) (2009) 455-460.

[69] N. Bergeon, A. Ramirez, L. Chen, B. Billia, J. Gu, R. Trivedi, Dynamics of interface pattern formation in 3d alloy solidification: first results from experiments in the declic directional solidification insert on the international space station, Journal of Materials Science 46(19) (2011) 6191-6202.

[70] V. Witusiewicz, U. Hecht, S. Rex, Top-view approach for in-situ observation of growth morphology in bulk transparent organic alloys, Journal of Crystal Growth 353 (2012) 17–24.

[71] S. Akamatsu, S. Bottin-Rousseau, M. Şerefoğlu, G. Faivre, Lamellar eutectic growth with anisotropic interphase boundaries: Experimental study using the rotating directional solidification method, Acta Materialia 60(6) (2012) 3206-3214.

[72] W. Huang, W. LiLin, Solidification researches using transparent model materials --- A review, Science China Technological Sciences 55(2) (2012) 377-386.

[73] W. Kurz, F. David, T. Rohit, Progress in modelling solidification microstructures in metals and alloys: dendrites and cells from 1700 to 2000, International Materials Reviews 64 (2018) 1-44.

[74] C. Beckermann, Modelling of macrosegregation: Applications and future needs, International Materials Reviews 47 (2002) 243-261.

[75] B. Drevet, H. Nguyen-Thi, D. Camel, B. Billia, M.D. Dupouy, Solidification of aluminum-lithium alloys near the cell/dendrite transition-influence of solutal convection, Journal of Crystal Growth 218(2-4) (2000) 419-433.

[76] R. Trivedi, S. Liu, P. Mazumder, E. Simsek, Microstructure development in the directionally solidified Al–4.0wt% Cu alloy system, Science and Technology of Advanced Materials 2(1) (2001) 309-320.

[77] H. Jamgotchian, N. Bergeon, D. Benielli, P. Voge, B. Billia, R. Guérin, Localized Microstructures Induced by Fluid Flow in Directional Solidification, Physical Review Letters 87(16) (2001) 166105.

[78] G. Reinhart, C.-A. Gandin, N. Mangelinck-Noël, H. Nguyen-Thi, J. Spinelli, J. Baruchel, B. Billia, Influence of natural convection during upward directional solidification: A comparison between in situ x-ray radiography and direct simulation of the grain structure, Acta Materialia 61 (2013) 4765–4777.

[79] F.L. Mota, Y. Song, J. Pereda, B. Billia, D. Tourret, J.-M. Debierre, R. Trivedi, A. Karma, N. Bergeon, Convection Effects During Bulk Transparent Alloy Solidification in DECLIC-DSI and Phase-Field Simulations in Diffusive Conditions, JOM Journal of the Minerals; Metals and Materials Society 69(8) (2017) 1280–1288.

[80] V. Witusiewicz, L. Sturz, A. Viardin, C. Pickmann, a.G. Zimmermann, Effect of convection on directional solidification in transparent succinonitrile–2.2wt, Acta Materialia 216 (2021) 117086.

[81] N. Bergeon, G. Reinhart, F.L. Mota, N. Mangelinck-Noël, H. Nguyen-Thi, Analysis of gravity effects during binary alloy directional solidification by comparison of microgravity and Earth experiments with in situ observation, European Physical Journal E 44(7) (2021).

[82] S. Akamatsu, S. Bottin-Rousseau, V.T. Witusiewicz, U. Hecht, M. Plapp, A. Ludwig, J. Mogeritsch, M. Şerefoğlu, N. Bergeon, F.L. Mota, L. Sturz, G. Zimmermann, S. McFadden, W. Sillekens, Microgravity studies of solidification patterns in model transparent alloys onboard the International Space Station, npj Microgravity 9(83) (2023).

[83] M.E. Glicksman, M.B. Koss, E.A. Winsa, Dendritic Growth Velocities in Microgravity, Physical Review Letters 73(4) (1994) 573-576.

[84] S. Akamatsu, H. Nguyen-Thi, In situ observation of solidification patterns in diffusive conditions, Acta Materialia 108 (2016) 325-346.

[85] I. Steinbach, Phase-field models in materials science, Modelling and Simulation in Materials Science and Engineering 17(7) (2009) 073001.

[86] N. Provatas, K.R. Elder, Phase-field Methods in Materials Science and Engineering, Wiley-VCH2010.

[87] A. Karma, W.-J. Rappel, Quantitative phase-field modeling of dendritic growth in two and three dimensions, Physical Review E 57(4) (1998) 4323-4349.

[88] A. Karma, Phase-Field Formulation for Quantitative Modeling of Alloy Solidification, Physical Review Letters 87(11) (2001) 115701.

[89] R. Folch, M. Plapp, Quantitative phase-field modeling of two-phase growth, Physical Review E 72(1) (2005) 011602.

[90] B. Echebarria, R. Folch, A. Karma, M. Plapp, Quantitative phase-field model of alloy solidification, Physical Review E 70(6) (2004) 061604.

[91] M. Plapp, 15 - Phase-Field Models, in: T. Nishinaga (Ed.), Handbook of Crystal Growth (Second Edition), Elsevier, Boston, 2015, pp. 631-668.

[92] N. Bergeon, D. Tourret, L. Chen, J.M. Debierre, R. Guérin, A. Ramirez, B. Billia, A. Karma, R. Trivedi, Spatiotemporal Dynamics of Oscillatory Cellular Patterns in Three-Dimensional Directional Solidification, Physical Review Letters 110(22) (2013) 226102.

[93] F.L. Mota, N. Bergeon, D. Tourret, A. Karma, R. Trivedi, B. Billia, Initial transient behavior in directional solidification of a bulk transparent model alloy in a cylinder, Acta Materialia 85 (2015) 362-377.

[94] J. Pereda, F.L. Mota, L. Chen, B. Billia, D. Tourret, Y. Song, J.M. Debierre, R. Guérin, A. Karma, R. Trivedi, N. Bergeon, Experimental observation of oscillatory cellular patterns in three-dimensional directional solidification, Physical Review E 95(1) (2017) 012803.

[95] F.L. Mota, J. Pereda, K. Ji, Y. Song, R. Trivedi, A. Karma, N. Bergeon, Effect of sub-boundaries on primary spacing dynamics during 3D directional solidification conducted on DECLIC-DSI, Acta Materialia 204 (2021) 116500.

[96] F.L. Mota, N. Bergeon, A. Karma, R. Trivedi, J.M. Debierre, Oscillatory-nonoscillatory transitions for inclined cellular patterns in three-dimensional directional solidification, Physical Review E 102(3) (2020).

[97] Y. Song, F.L. Mota, D. Tourret, K. Ji, B. Billia, R. Trivedi, N. Bergeon, A. Karma, Cell invasion during competitive growth of polycrystalline solidification patterns, Nature Communications 14(1) (2023) 2244.

[98] D. Tourret, J.M. Debierre, Y. Song, F.L. Mota, N. Bergeon, R. Guérin, R. Trivedi, B. Billia, A. Karma, Oscillatory cellular patterns in three-dimensional directional solidification, Physical Review E 92(4) (2015) 042401.

[99] J. Pereda, F.L. Mota, J.M. Debierre, B. Billia, R. Trivedi, A. Karma, N. Bergeon, Experimental characterization and theoretical analysis of cell tip oscillations in directional solidification, Physical Review E 102(3) (2020) 032804.

[100] F.L. Mota, M. Medjkoune, L.S. Littles, A. Karma, N. Bergeon, Solidification furnace for in situ observation of bulk transparent systems and image analysis methods, Review of Scientific Instruments 94(6) (2023).

[101] H. Weidong, G. Xingguo, Z. Yaohe, Primary spacing selection of constrained dendritic growth, Journal of Crystal Growth 134(1) (1993) 105-115.

[102] D. Tourret, A. Karma, Multiscale dendritic needle network model of alloy solidification, Acta Materialia 61(17) (2013) 6474-6491.

[103] D. Tourret, A. Karma, Growth competition of columnar dendritic grains: A phase-field study, Acta Materialia 82 (2015) 64-83.

[104] R. Trivedi, N. Bergeon, B. Billia, B. Echebarria, A. Karma, S. Liu, N. Mangelinck, C. Weiss, In situ characterization of interface-microstructure dynamics in 3D-Directional Solidification of model transparent alloys, Microgravity - Science and Technology 16(1) (2005) 133-137.

[105] A.J. Clarke, D. Tourret, Y. Song, S.D. Imhoff, P.J. Gibbs, J.W. Gibbs, K. Fezzaa, A. Karma, Microstructure selection in thin-sample directional solidification of an Al-Cu alloy: In situ X-ray imaging and phase-field simulations, Acta Materialia 129 (2017) 203-216.

[106] D. Tourret, A.J. Clarke, S.D. Imhoff, P.J. Gibbs, J.W. Gibbs, A. Karma, Three-Dimensional Multiscale Modeling of Dendritic Spacing Selection During Al-Si Directional Solidification, JOM 67(8) (2015) 1776-1785.

[107] B. Echebarria, A. Karma, S. Gurevich, Onset of sidebranching in directional solidification, Physical Review E 81(2) (2010) 021608.

[108] K.B. Glasner, Nonlinear preconditioning for diffuse interfaces, Journal of Computational Physics 174 (2001) 695-711.

[109] K. Ji, A.M. Tabrizi, A. Karma, Isotropic finite-difference approximations for phase-field simulations of polycrystalline alloy solidification, Journal of Computational Physics 457(1) (2022) 111069.

[110] D. Tourret, Y. Song, A.J. Clarke, A. Karma, Grain growth competition during thin-sample directional solidification of dendritic microstructures: A phase-field study, Acta Materialia 122 (2017) 220-235.

[111] W.W. Mullins, R.F. Sekerka, Stability of a Planar Interface During Solidification of a Dilute Binary Alloy, Journal of Applied Physics 35(2) (1964) 444-451.

[112] W.A. Tiller, K.A. Jackson, J.W. Rutter, B. Chalmers, The redistribution of solute atoms during the solidification of metals, Acta Metallurgica 1(4) (1953) 428-437.

[113] M.E. Glicksman, N.B. Singh, Effects of crystal-melt interfacial energy anisotropy on dendritic morphology and growth kinetics, Journal of crystal growth 98(3) (1989) 277-284.

[114] M. Muschol, D. Liu, H.Z. Cummins, Surface-tension-anisotropy measurements of succinonitrile and pivalic acid: Comparison with microscopic solvability theory, Physical Review A 46(2) (1992) 1038-1050.

[115] X. Feng, B.B. Laird, Calculation of the crystal-melt interfacial free energy of succinonitrile from molecular simulation, (0021-9606 (Print)).

FIGURES :

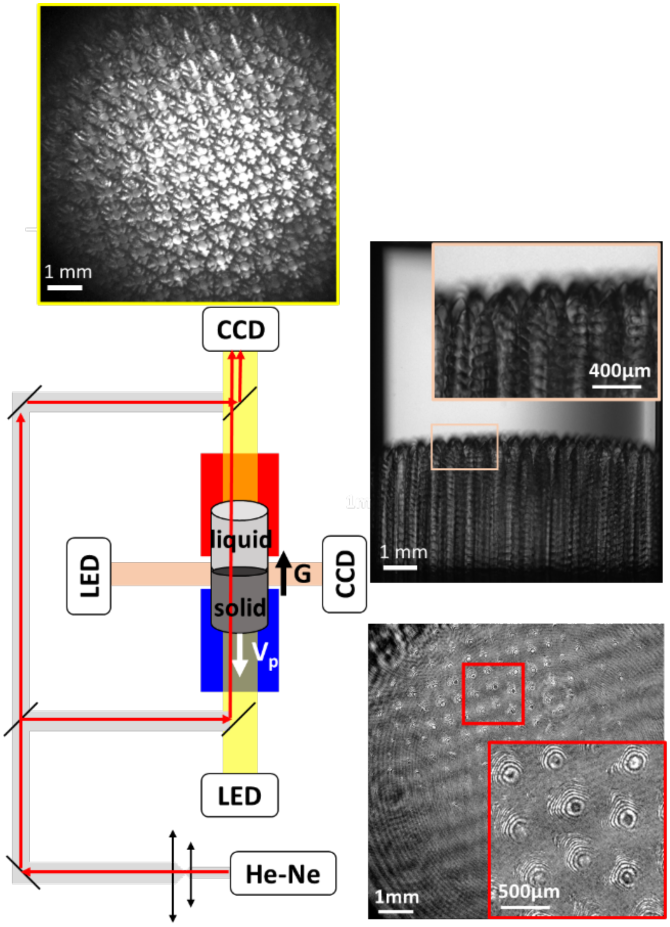

Fig. 1. Schematic representation of the DECLIC-DSI apparatus and its optical modes. From top to bottom: axial direct; transverse direct and axial interferometric. The red and blue rectangles represent the hot and cold zones of the Bridgman furnace.

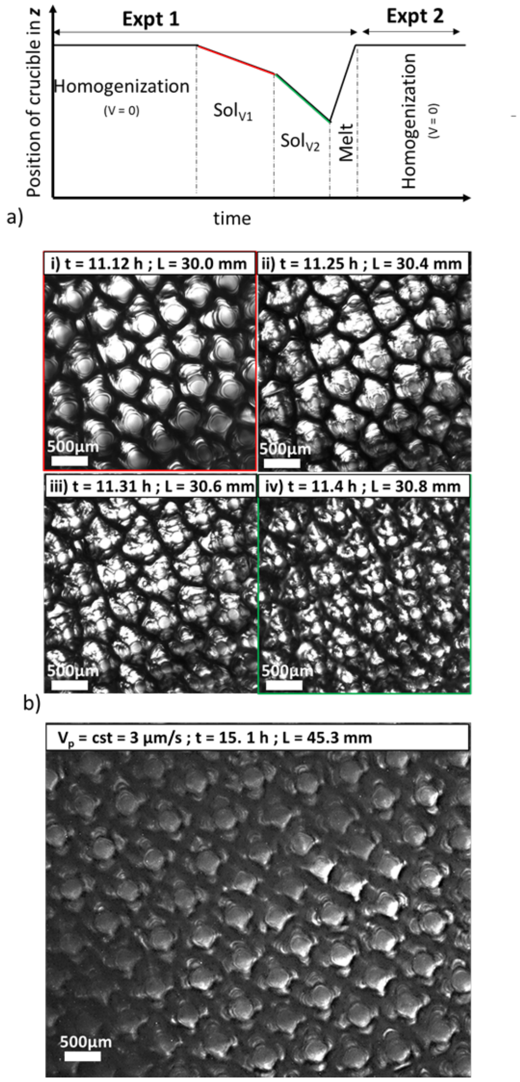

<u>Fig. 2.</u> a) Schematic representation of the stages in a pulling velocity jump experiment. b) Real time images of a sequence of evolution of the dendritic pattern (SCN-0.46 wt.% camphor, G = 12 K/cm), zoomed in the central grain, around the velocity jump from $V_{p,1}$ = 0.75 µm/s to $V_{p,2}$ = 3 µm/s; i) final state of the first solidification stage at V_p = 0.75 µm/s; L = 30.0 mm, ii) V_p = 3 µm/s; L = 30.4 mm, iii) V_p = 3 µm/s; L = 30.6 mm, iv) V = 3 µm/s; L = 30.5 mm. (SCN-0.46 wt.% camphor; G = 12K/cm). c) Top view *in situ* image of dendritic pattern solidifying at V_p = 3 µm/s in a constant pulling velocity experiment. (SCN-0.46 wt.% camphor; L = 45.3 mm; G = 12K/cm).

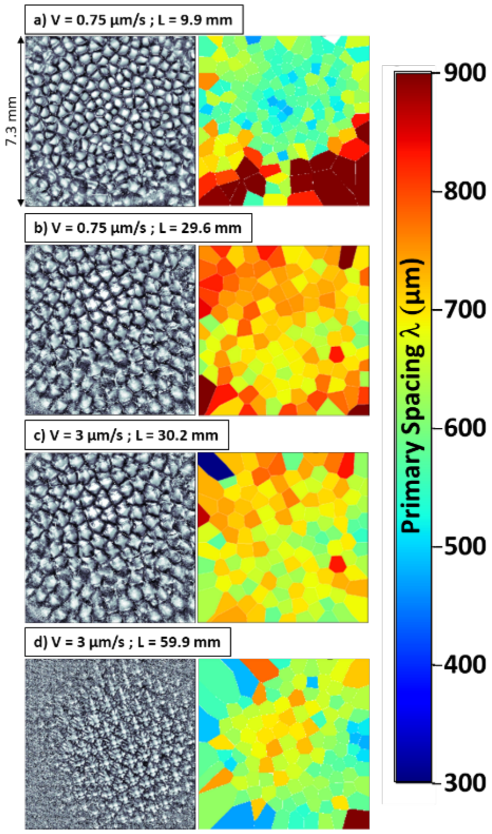

Fig. 3. Top view images and tessellation analysis of the pattern in experiment *A* (from 0.75 to 3 μm/s) at the start and end of each solidification stage and their corresponding primary spacing map. (SCN-0.46 wt% camphor; G = 12K/cm)

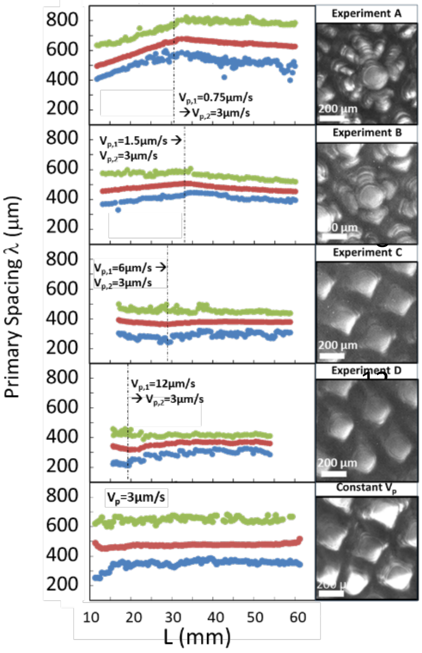

Fig. 4. Left, graphs with minimum (blue - λ_{min}), average (red - λ_{ave}) and maximum (green -λ_{max}) primary spacing evolution on the main central grain. Right, typical morphology of a dendrite in steady state at 3 µm/s. (SCN-0.46 wt% camphor; G = 12 K/cm)

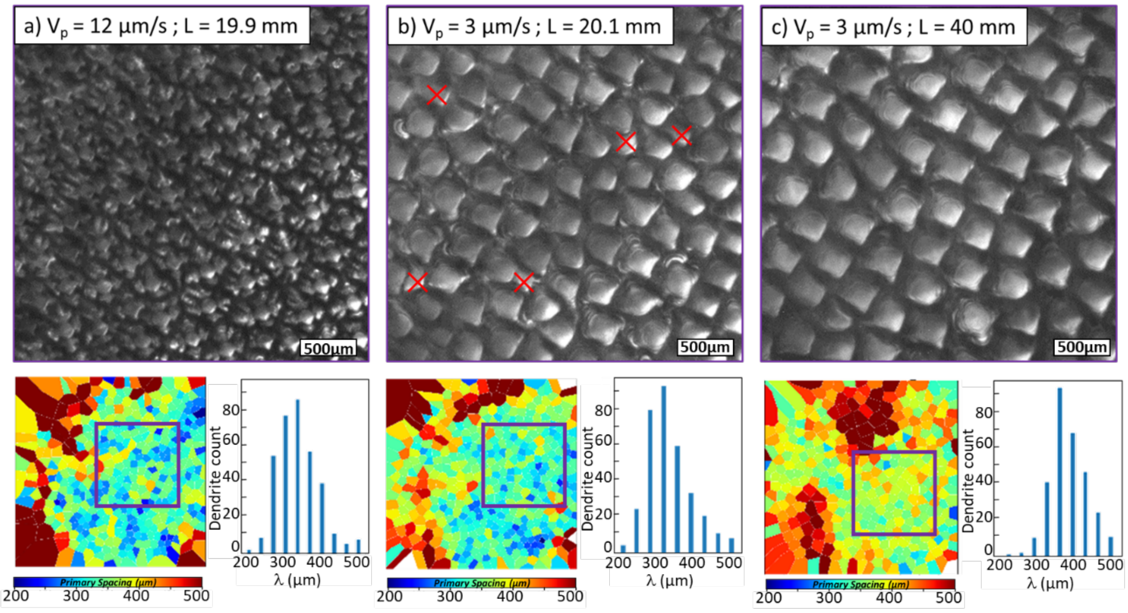

Fig. 5. Top view images of the pattern zoomed in the main grain (purple rectangle) and the corresponding primary spacing map and distribution in histogram (for the whole interface) for a) the final state of experiment *D* at V_p = 12 µm/s, L = 19.9 mm; b) the initial state of experiment *D* at V_p = 3 µm/s, L = 20.1 mm; and c) the steady state of experiment *D* at V_p = 3 µm/s, L = 40 mm. The red crosses in b) correspond to the soon-to-be eliminated dendrites. (SCN-0.46wt% camphor; G = 12K/cm)

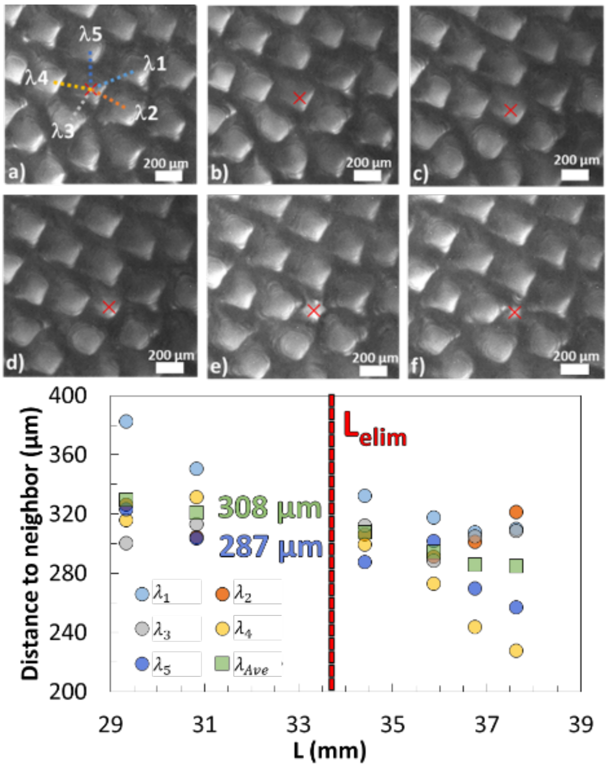

Fig. 6. a)-f) Top view images of a sequence of a dendrite elimination at V_p = 3 µm/s. λ_i is the distance between the soon-to-be eliminated dendrite and its neighbors. g) Distance to neighbor as a function of the solidification length. a) L = 29.4 mm, b) L = 30.9 mm, c) L = 34.3 mm, d) L = 35.8 mm, e) L = 36.7 mm, f) L = 37.6 mm. (SCN–0.46wt% camphor; G = 12K/cm)

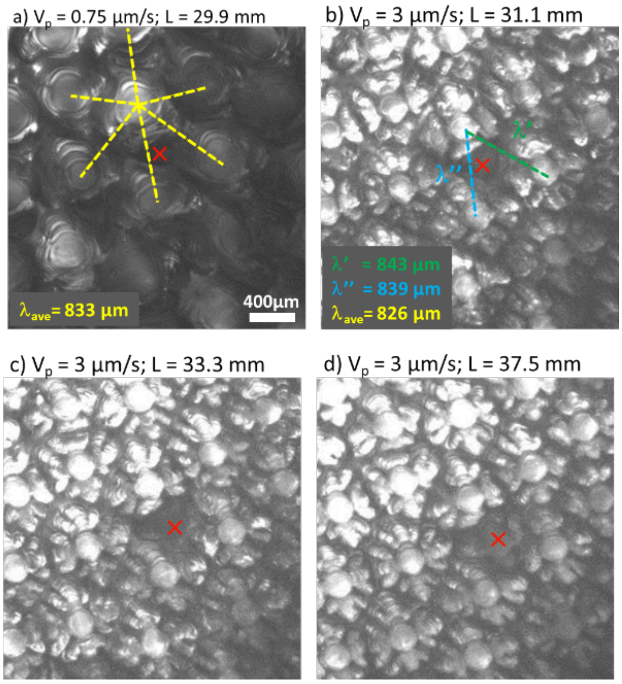
a) V_p = 0.75 µm/s; L = 29.9 mm
b) V_p = 3 µm/s; L = 31.1 mm
c) V_p = 3 µm/s; L = 33.3 mm
d) V_p = 3 µm/s; L = 37.5 mm

Fig. 7. Sequence of the formation of a new dendrite by tertiary branching. a) V_p = 0.75 µm/s, L = 29.9 mm; b) V_p = 3 µm/s, L = 31.1 mm; c) V_p = 3 µm/s, L = 33.3 mm; d) V_p = 3 µm/s, L = 37.5 mm. (SCN-0.46wt% camphor, G = 12K/cm)

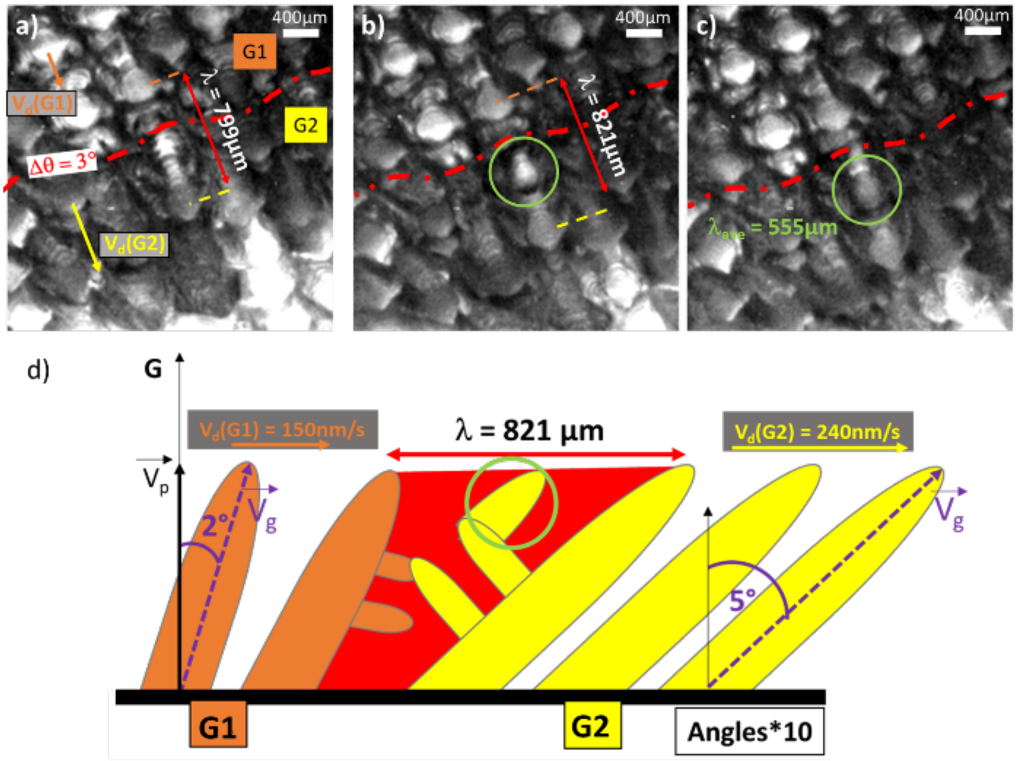

<u>Fig. 8.</u> Sequence of formation of a new dendrite by tertiary branching at $V_p = 3$ μm/s in a region of sub-boundary between sub-grains G1 and G2 misoriented by about 3°. λ corresponds to the distance between the dendrite (in G2) that generates the new dendrite and the closest dendrite along the direction of the secondary branch (dotted white line). a) t = 0 s; b) t = 319 s; c) t = 951 s; d) schematic 2D section along the white dotted line. (SCN-0.46 wt% camphor; G = 12K/cm).

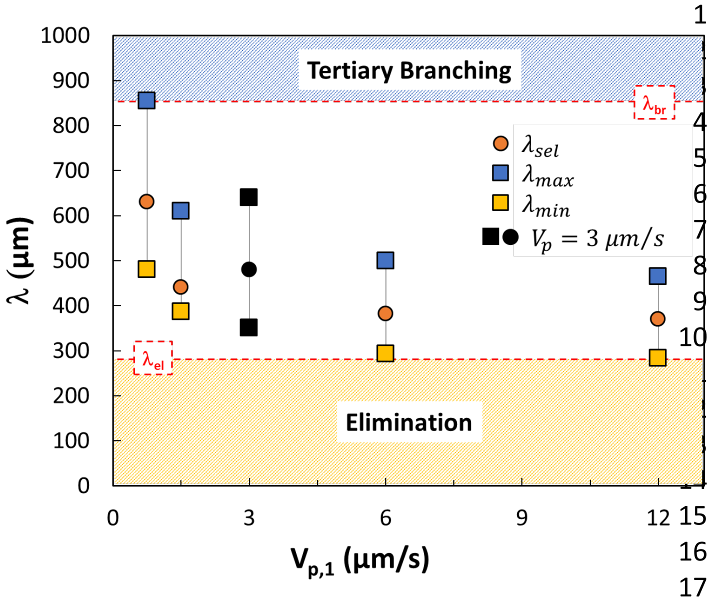

Fig. 9. Accessible ranges of primary spacing at 3 µm/s after each experiment. The tertiary branching and elimination instabilities correspond to the limits of the accessible range and define the stability band limits. (SCN-0.46 wt% camphor, G = 12K/cm)

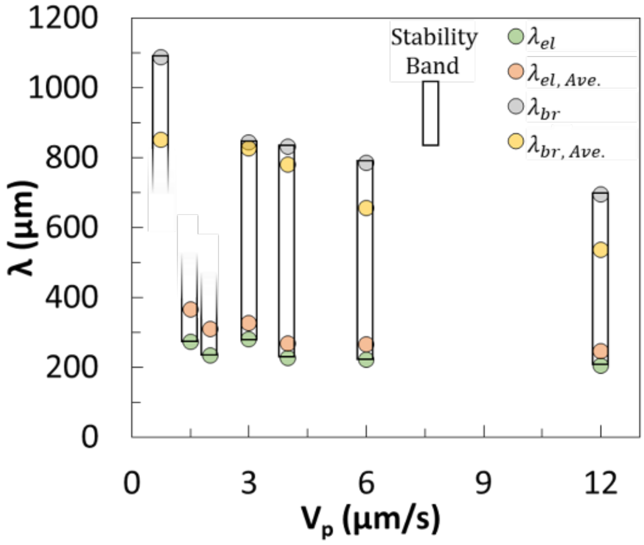

Fig. 10. Summary of primary spacing stability band observed for solidification velocities of 0.75, 1.5, 2, 3, 4, 6 and 12 µm/s (SCN-0.46wt% camphor; G = 12 K/cm). The tertiary branching and elimination limit measured with average distance between neighbors dendrites are represented by $\lambda_{br,\ Ave.}$ and $\lambda_{el,\ Ave.}$ while thresholds manually measured are λ_{br} and λ_{el}.

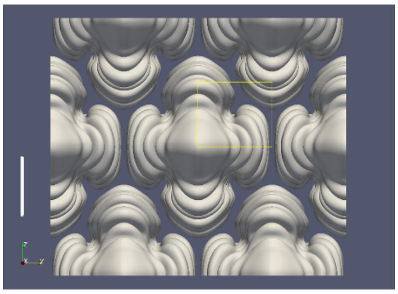

Fig. 11. Phase-field simulation displaying the hexagonal packing of dendrites in SCN-0.46wt% Camphor, G = 12.5 K/cm, V = 1.5 µm/s. The simulation domain is highlighted by the yellow rectangle. The sidebranch grows along z = 0 in the positive z direction and continues its growth after it reaches the boundary in the negative z at y = L_y. Through reflections and translations of the simulated domain a full dendrite and its six nearest neighbors are constructed. The white scale bar is equal to 200 µm.

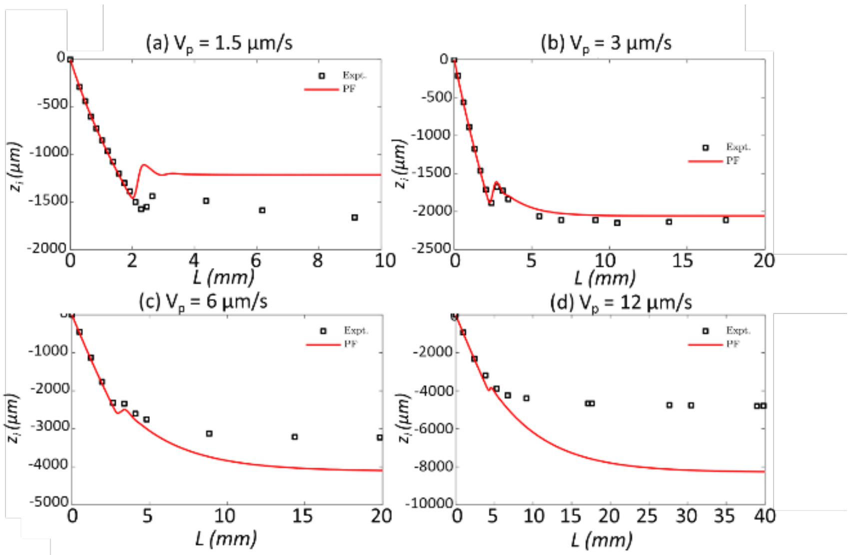

Fig. 12. Interface dynamics measured in the experiment and compared to PF simulations with 1D-TFC, for V$_p$ (µm/s) = 1.5 (a), 3 (b), 6 (c), and 12 (d). (G = 12.5 K/cm)

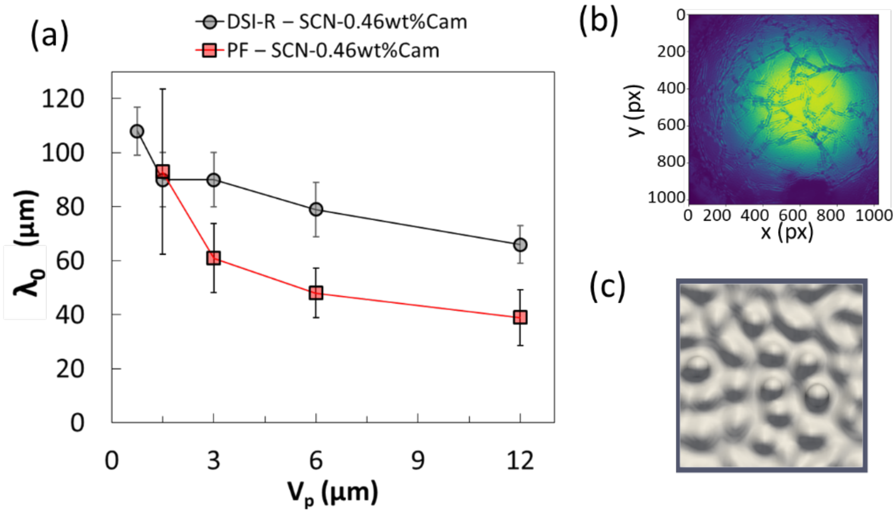

Fig. 13. (a) Initially selected spacing λ_0 as a function of pulling velocity V_p: measured average initial spacings in the experiments, and in PF simulations using the TFC. Interface morphologies at the time of the initial breakdown of the planar interface used to measure λ_0 in experiment (b) and PF simulation (c) for V_p=3 μm/s and G=12 K/cm. The simulation domain is 305 μm x 305 μm in (c).

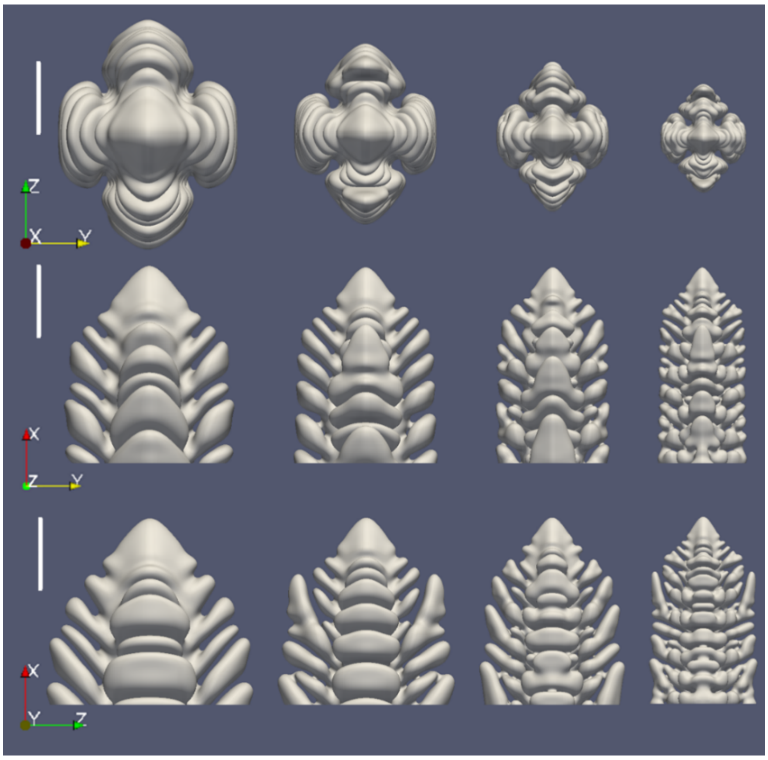

Fig. 14. Phase-field simulations of dendrites at their maximum spacing in SCN-0.46wt% Camphor, G = 12.5 K/cm, and pulling velocities of 1.5, 3, 6, and 12 μm/s from the left column to the right column. The top row looks down the x-axis, the middle row shows the y-domain, and the bottom row shows the z-domain. All simulated dendrites share the same scale where the white bar to the left is equal to 200 μm.

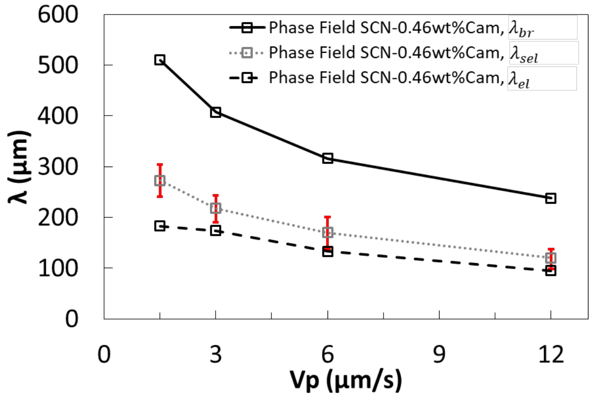

Fig. 15. The stable spacing band predicted by phase-field simulations over different pulling velocities defined by the tertiary overgrowth and elimination thresholds. The red bars around the dynamically selected spacing represent λ_{min} and λ_{max}.

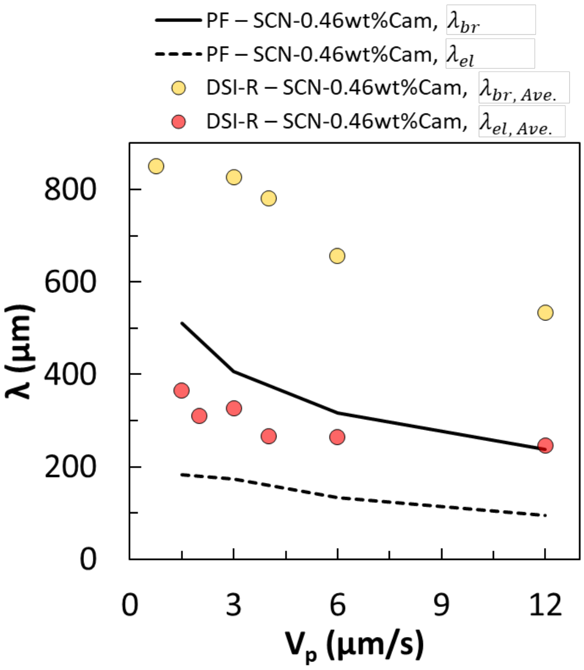

Fig. 16. The stable spacing band predicted by phase-field compared to the observed DSI-R elimination and tertiary branch instability averages.

TABLES:

Table 1: Summary of the minimum, average and maximum primary spacings (respectively λ_{min}, λ_{ave} and λ_{max}) for each experiment at each step of solidification. i1 : start of analyzable data at $V_{p,1}$, f1 : end of solidification at $V_{p,1}$, i2 : start of solidification at $V_{p,2}$; f2 : end of solidification at $V_{p,2}$.

Run	V_p ($\mu m/s$)	Step	Length (mm)	λ_{min} (μm)	λ_{ave} (μm)	λ_{max} (μm)
A	$V_{p,1} = 0.75$	i_1	9.8	410	498	596
		f_1	29.9	587	679	818
	$V_{p,2} = 3$	i_2	32.3	567	679	855
		f_2	59.9	526	629	786
B	$V_{p,1} = 1.5$	i_1	10.8	374	462	574
		f_1	29.7	431	510	587
	$V_{p,2} = 3$	i_2	33.2	443	510	592
		f_2	59.8	400	458	522
C	$V_{p,1} = 6$	i_1	15.9	298	391	743
		f_1	29.9	246	370	484
	$V_{p,2} = 3$	i_2	33.1	264	369	488
		f_2	59.7	312	381	440
D	$V_{p,1} = 12$	i_1	15.5	240	348	462
		f_1	19.9	226	320	423
	$V_{p,2} = 3$	i_2	23.9	229	339	435
		f_2	59.7	318	373	446

Table 2: Overview of instabilities at various velocities, their locations, frequency of events, and corresponding experiments. MG: Main Grain, SGB: Sub-grain Boundary.

Threshold	Velocity	$V_{p,1}$	$V_{p,2}$	Events	Location
Branching	0.75 µm/s	0.75	3	1	MG
	3 µm/s	0.75	3	1	MG
		12		3	SGB
	4 µm/s	2	4	5	SGB
	6 µm/s	12	6	5	SGB
	12 µm/s	12	6	6	SGB
			3	5	SGB
Elimination	1.5 µm/s	12	1.5	8	MG/SGB
		6		4	MG/SGB
	2 µm/s	2	4	7	MG/SGB
			2	8	MG/SGB
		4		6	MG/SGB
	3 µm/s	12	3	4	MG/ SGB
		6		7	MG
	4 µm/s	2	4	7	MG/SGB
		4	2	5	SGB
	6 µm/s	1.5	6	7	MG/SGB
		12		4	SGB
		6		10	MG
	12 µm/s	12	3	4	SGB
			6	6	SGB

Table 3: Simulation parameters that depend on either velocity or interface thickness.

V_p (µm/s)	1.5	3	6	12
W/d_0	185	176	151	108
Δt (s)	0.0036	0.0033	0.0024	0.0012
L_x (µm)	2030.78	1302.52	1494.98	977.55